# Electrochemical behaviour of austenitic stainless steel under tribological stresses and irradiation

Bernard Normand, Nicolas Bererd, Philippe Martinet, Sabrina Marcelin, Moustapha Moine, José Feirrera, Dominique Baux, Thierry Sauvage, Nathalie Moncoffre

# Electrochemical behaviour of austenitic stainless steel under tribological stresses and irradiation

Bernard Normand[1*], Nicolas Bererd[2,3], Philippe Martinet[2], Sabrina Marcelin[1], Moustapha Moine[1], José Feirrera[1], Dominique Baux[4], Thierry Sauvage[4], Nathalie Moncoffre[2]

[1]Université de Lyon, INSA Lyon, MATEIS UMR 5510 CNRS, Villeurbanne cedex, France
[2]Université de Lyon, IP2I UMR 5822 CNRS Villeurbanne, France
[3]Université de Lyon, IUT Lyon 1-département de chimie, Villeurbanne, France
[4]CNRS, CEMHTI UPR 3079, Université d'Orléans, Orléans, France

*Corresponding author
*B. Normand*
*Campus LyonTech-La Doua*
*20 avenue Albert Einstein 69621 Villeurbanne cedex, France.*
*Tel. +33 (0)4 72 43 62 87,*
bernard.normand@insa-lyon.fr

## Abstract

An experiment was developed to characterise the behaviour of 316L stainless steel under the combined effects of corrosion, tribology, and irradiation. This original experiment shows that radiolysis, through the production of free radicals and $H_2O_2$, leads to an oxidising medium. The electrochemical behaviour of the material from the recorded polarisation curves and electrochemical impedance spectroscopy measurements indicates that the passive film under irradiation is a Cr oxi-hydroxide layer. The layer has more formative thickness under irradiation. When the irradiation is interrupted, the passive film is identical to that observed before irradiation. The repassivation is faster during irradiation and friction.

## Key words:

A: Stainless steel, B: Polarisation, Electrochemical Impedance Spectroscopy, C: Passive film, Tribocorrosion, Irradiation.

## Highlights

- A new device for tribocorrosion under irradiation has been developed.
- Radiolysis makes the medium more oxidising.
- The film formed on a 316L sample is thicker under irradiation.
- After irradiation, the passive film is the same as before the irradiation.
- The repassivation occurring after application of sliding is faster under irradiation.

## 1. Introduction

Austenitic stainless steel materials are often used in structural applications, where they have to undergo mechanical stresses. Thus, they must possess relatively good mechanical as well as corrosion resistance properties in the environment where they are used. Moreover, their reactivity has to be taken into account. Numerous studies exist on stress corrosion [**1**], fatigue corrosion [**2**], and hydrogen embrittlement [**3**] of these materials. More recently, some studies related to superficial stresses on stainless steel materials have also been reported [**4**]. The concept related to the effect of a combination of tribology and corrosion (known as tribocorrosion) has also been explored [**5**].

However, nuclear field is one of the areas in which the occurrence of tribocorrosion can be very risky. Indeed, several tribosystems, cited in [**6**], have been identified where large displacements and fretting phenomena have occurred. For example, the power developed by a nuclear reactor is controlled by managing the rod cluster control assemblies (RCCAs) that contain neutron-absorbing elements. This arrangement is controlled by the control rod drive mechanism (CRDM), guided by control rod guidance assemblies (CRGAs), as presented in **Figure 1**.

All these devices are immersed in the reactor and are subject to vibrations. As shown in **Figure 2**, the 304L rod is guided by a 316L plate hardened with ion nitriding [**4**]. This treatment comprises a superficial diffusion of nitrogen into the stainless steel to limit the wear.

In this study, the development of this device was first studied from a tribological viewpoint, which involves the hardening of the surface to limit the wear. Then, in the second step, a corrosionist point of view was considered that takes into account the effect of nitrogen on the maintenance of the passive properties of the austenitic stainless steel. Further, for optimising the process, this previous work guided the quantity of nitrogen content to be introduced to avoid the formation of nitride, which is very critical to corrosion resistance [**7**]. However, the

cited study considered a mechanical approach and followed it with a physico-chemical approach, which is sub-optimal for studying the multifunctional behaviour of materials. Simultaneously considering the mechanical and physico-chemical stresses is important to assess their synergistic effects. Consequently, scale 1 simulators (MAGALY and AURORE) were developed by Framatome that allow the material to be loaded under conditions more representative of reactor operations [**6**]. These simulators are remarkable and can handle great complexities, besides facilitating the simulation of real-world contact conditions in terms of load, kinetics, and environment. However, as these simulators do not allow a combination of electrochemical measurements and irradiation effect testing, all the constraints involved in nuclear energy production are not completely represented. Electrochemical measurements are essential to study the evolution of the reactivity of the material exposed in the aqueous medium and subjected to superficial stresses. These measurements, associated with the characteristics of wear, can provide more holistic information on the synergistic effects of wear and corrosion [**8**], and the objective of such fields of study is to quantify the wear accelerated by corrosion and vice versa [**9**]. Notably, this type of damage is mainly observed on materials that can reach a passive state, such as stainless steel [**10**].

Austenitic stainless steel is protected by a thin film of a few nanometers thickness that develops on its surface [11]. The passive film is initially air-formed and can be modified in terms of composition and thickness depending on the nature of the electrolyte in which the stainless steel is immersed. When the stainless steel substrate is subjected to sliding contact or impact, the passive film can get damaged leading to the exposure of the underlying material, which can dissolve in the solution. The dynamics of the contact compete with the reconstruction kinetics of the passive film, also called the repassivation phenomenon [**12, 13**]. To this, one must add the fact that the load causes microstructural modifications in the rubbed/impacted surface, resulting in a tribologically transformed surface [**14, 15**].

Consequently, this worn surface has a different reactivity than the unaffected surface of the material, which is the whole issue of tribocorrosion in general. The importance of this issue deserves particular attention and motivates this work.

Although, as mentioned above, earlier works have also tried to identify the risk factors associated with damage due to tribocorrosion [**6**], the present work aims to introduce electrochemical measurements of the friction device to quantify the observations already made. Moreover, for an even wider representation, irradiation effects have also been added to the considerations.

The effects of irradiation on corrosion are collectively known as irradiation assisted stress corrosion cracking (IASCC), which is considered as a special case of corrosion under stresses assisted by irradiation, and is characterised by intergranular cracking on one hand and a loss of ductility on the other [**16**]. The damage is attributed to a microstructural and chemical evolution of the solid material (irradiation effect) and the radiolysis of the liquid medium (chemical effect) [**17**]. The work of Bruemmer et al. illustrated the effects of a neutron beam fluence on the microstructural modifications in a 304 steel sample and the consequences of the modifications on IASCC behaviour [**18**]. The microstructural evolution of materials is due to the displacement of atoms, and each displacement produces a combination of an interstitial atom and a vacancy, together called a Frenkel pair. It is mainly the displacement of these point defects that gives rise to dislocation loops, precipitation, segregation, and local chemical evolutions (inverse Kirkendall segregation, interstitial association segregation) that characterise the irradiation damages. The latter processes also lead to a local enrichment or depletion of alloying elements (including chromium), which contributes to the weakening of the passive film that protects the stainless steel and to a loss of the steel's mechanical properties [**19**].

At this stage of knowledge, the analyses of passive films under irradiation, or only exposed to a fluid having undergone radiolysis phenomena, practised on a 316L, exposed to conditions representative of the nuclear environment (320°C, 3 wppm H2, neutral pH), show significant modifications of the passive film. This work indicates a chromium depletion in the internal part of the passive film of spinel oxides type and the presence of hematite on the surface of the oxide, which indicates the oxidizing power of the solution during or after irradiation [**20**]. This phenomenon is less marked when the material is passivated before radiolysis. Physicochemical analyses indicate that passive films are thinner and more porous under the effect of proton irradiation, which gives them poorer corrosion resistance properties [**21**].

In our work, the results obtained do not show such variations in the passive film. In these references the exposures of materials to irradiation are carried out over periods of 24 to 72 hours, in our case we expose our systems over a very short period, the time of an impedance or friction measurement, that is to say between 20 and 35 minutes maximum.

Radiolysis, on the other hand, leads to a modification in the redox potential of the medium due to the production of free radicals ($H^{\bullet}$, $O^{\bullet}$, $OH^{\bullet}$, $e^{-}_{aq}$, etc.) and their recombination under $H_2$ and $H_2O_2$ **[22]**, which can lead to an evolution of the passive film [**23**]. Hence, an $H_2$ overpressure is added in the Pressurised Water Reactor (PWR) to maintain a potential lower than -230 mV vs NHE (Normal Hydrogen Electrode), to prevent the production of oxidising radicals and the associated increase in potential and thereby the occurrence of SCC in stainless steel materials **[24, 25]**.

**Figure 3** illustrates the different themes to be considered for achieving synergy among the different possible demands of the nuclear field. It demonstrates the interactions between (1) tribology and corrosion, (2) corrosion and irradiation, and (3) tribology and irradiation. The fourth and final interaction represents tribocorrosion under irradiation, which is addressed in this paper.

To summarise, in this study we present an original experiment to jointly characterise the interactions between tribology and corrosion under irradiation and then discuss the resultant modifications in the properties of the passive film under the irradiation and its ability to reform after a tribological event. This paper is divided into two parts: the first presents the experiments and related activities performed in this study; the second presents the results obtained from the experiments.

This work can be considered as a preliminary study to prove the feasibility of such complex research that focuses on a systemic approach to quantifying the multifunctionality of nuclear materials. It is of course aimed at nuclear applications, but the subject being so complex, we first chose to validate in this paper the feasibility of our study by working on a more conventional solution, for which we have a great deal of data concerning passive materials.

## Material and methods

### 1.1. Material

A commercial austenitic steel material (316L type) supplied by GoodFellow, and composed of C (0.02 wt%), Si (0.49 wt%), S (0.001 wt%), P (0.035 wt%), Mn (1.79 wt%), Ni (10.1 wt%), Cr (16.7 wt%), Mo (2.03 wt%), balanced with Fe, was used in this study.

A 500 µm thick sheet of the selected steel type was chosen as the study sample. The particular thickness was chosen to allow the irradiating proton beam to pass through the sample and stop close to the metal/solution interface.

### 1.2. Electrochemical measurements

Electrochemical technics were employed in this work because they enable us accurately capture the evolution of the 316L stainless steel/electrolyte interface properties. For example, electrochemical impedance spectroscopy is an especially sensitive technic which allows us to access the properties of the passive film over potential, particularly in terms of thickness.

All electrochemical measurements were recorded in an aerated 0.02 mol/L $Na_2SO_4$ solution (50 mL), maintained at 20°C without stirring. The electrochemical cell comprised three

electrodes: the working electrode, which included the 316L thin sheet fixed in the tribocorrosimeter, with an exposed surface of 12.5 cm²; the counter electrode, which was a porous carbon stick (26 cm²); and the reference electrode, a mercury sulphate electrode (MSE). This conventional three-electrode device was controlled with a Ref600 type potentiostat distributed by Gamry.

To ensure the reproducibility of the electrochemical measurements, the surface of the material was subjected to a preliminary electrochemical protocol to reduce the air-formed passive film that may have developed during sample storage. The preparatory protocol included an Open Circuit Potential (OCP) measurement for 600 s, followed by a applied potential of -1.5 V/MSE for 600 s to reduce the passive film formed in the air. This was followed by an OCP measurement for 600 s to relax the cathodically polarised surface and finally a polarisation of -330 mV/MSE for 3600 s. After this conditioning, the sample was left at OCP for one hour. The polarisation value of -330 mV/MSE was chosen because it corresponds to the potential achieved by the material when immersed in the solution for 48 h. Thus, this value corresponds to the corrosion potential of the material in the passivated state, immersed in the neutral and aerated sulphate solution used in this study.

After the *in situ* electrochemical surface preparation of the 316L sample, the evolution of the corrosion potential (with OCP measurements) and the polarisation curves (I = f(E)) were recorded. The OCP measurement provides information on the oxidation-reduction potential between the material and the solution and identifies the evolutionary cycles of the stainless steel surface. The measured values tend toward passivation when the potential increases, or toward corrosion when the potential decreases significantly. The polarisation curve supplied informations regarding the involved reaction mechanisms and their kinetics, and the current densities involved and their range of existence from the potentials [**26**]. The potential scanning rate for the polarisation curve plotting was set as 1 $mV.s^{-1}$ to ensure the reversibility of the

188 measurement, and the potential scan limits were set as -0.5 V/OCP in the cathodic range and
189 +1.5 V/OCP in the anodic range.
190 As the 316L austenitic stainless steel is a passive material, studying the evolution of the
191 passive film and its resistivity at the 316L/passive film/electrolyte interfaces *in situ* and in the
192 presence of irradiation is also of interest. These observations could only be obtained thanks to
193 electrochemical impedance spectroscopy. This technic is based on the power-law model,
194 which has proved its relevance in characterising the properties of passive films [**27, 28, 29,**
195 **30**]. However, the material must be under stationary state for successfully obtaining the
196 electrochemical behaviour measurements; therefore, they were performed without any
197 friction. The electrochemical impedance measurements were acquired at the corrosion
198 potential with an amplitude of 25 mV, respecting the linearity condition of the signal. The
199 impedance diagrams were obtained over a frequency range of 100 kHz to 5 mHz with 8 pts
200 per decade.
201 Thereafter, the measurements were retaken during friction, when the metal/solution
202 interface is considered to be in a non-stationary state. The displacement of the pin
203 depassivated the surface of the material, resulting in potential and current transients, which
204 were measured with the electrochemical noise (EN) technic under ZRA mode monitored by
205 using a Ref 600 potentiostat. The EN data were acquired sequentially with 100 Hz as the
206 sampling frequency, filtered at 1% with the ESA 410 software. The analysis of these
207 transients provided information on the repassivation time constants extracted from the model.
208 **2.3. Irradiation conditions**
209 Irradiation was applied to a CEMHTI UPR 3079 CNRS cyclotron with a 16 MeV proton
210 beam ($H^+$). During their path to reach the electrochemical cell, the protons loses energy
211 passing through two titanium foils (27 µm each) of the ionization chamber, the titanium exit
212 foil (27 µm) at the beam line end and the 316L stainless steel sample. The energy loss in air

between the Ti exit foil and the sample is considered as negligible. The energy at the entrance side of the sample is 15,2 MeV. Its thickness is reduced to 500 µm to ensure a total transmission of the incident protons through the sample. An energy of 2.9 ±0.5 MeV was transferred to the solution. The energy can be calculated to such near precision in these conditions thanks to the SRIM code **[31]**, which postulates that protons stop at a distance equal to approximately 140 ±40 µm above the interface (**Figure 4**). During all of the experiments, the protons flux impinging the sample is monitored by the ionization chamber to obtain a constant dose rate in the solution. The ionization chamber current is calibrated by a Faraday cup and its calibration verified before and after the irradiation. The beam size was 8 mm in diameter, providing a scanning area of 50 mm². The beam current was fixed to 10 or 40 nA, giving rise to a flux of $1.2x10^{11}$ ion.cm$^{-2}$.s$^{-1}$ or $5x10^{11}$ ions.cm$^{-2}$.s$^{-1}$, respectively. These low values of current are mandatory to minimize the activation of steel samples induced by protons. The duration of irradiation varied according to the electrochemical measurements, considered cyclical or not. It was between 20 min and 10 hours, resulting in doses deposited in the solution (50mL) ranging from 1.3 kGy to 167 kGy. The equivalent dose rate, due to sample activation after 30 min of irradiation is about 100 µSv/h, making rapid *ex situ* and *post mortem* surface analysis difficult.

It must be noted that all results presented in this paper do not come from the same cyclotron run which explains differences in the corrosion potential values under irradiation. For each run, the corrosion potential value has been measured as a blank.

### 2.4 Tribological procedure

To apply the frictional stresses, the required tribocorrosimeter that could be adapted for installation on one beam line of the CEMHTI cyclotron was first developed. **Figure 5** shows the functional diagram of the developed apparatus along with the specifications of its various

components. The on-site tribocorrosion device installed on the cyclotron is presented in **Figure 6**. Friction was provided with a chemically inert alumina pin of 12 mm diameter, which ensured a reciprocating displacement of 8 mm (+/- 4 mm). Sample is immersed during 14h before sliding. An idle time of 6 s was ensured after each pin displacement to allow time for the material to repassivate. The displacement rate of the pin was 8 $mm.s^{-1}$. The number of performed cycles was between 600 and 1000. According to Hertzian considerations, the maximum shear stress was 450 MPa and the maximum shear depth was 20 µm.

## 2. Results and discussion

### 3.1 Irradiation effect on the passive film

**Figure 7** shows the evolutionary stages of the potential of 316L stainless steel immersed in $Na_2SO_4$ solution. After undergoing the preparation protocol, the material quickly reaches a stable potential close to -430 mV/MSE. The polarisation curves later confirmed that this is the potential that characterises the passivated state of the austenitic stainless steel. When the corrosion potential reaches a steady state, the proton irradiation beam is switched on, which causes an instant increase in the potential to a more anodic value close to -320 mV/MSE. This potential remains constant for the duration the beam remains active. When the irradiation is interrupted, the potential further ennobles to attain a value close to -290 mV/MSE and then slowly drops after 5 min of latency to reach a corrosion potential close to the one recorded during the application of the beam. At this stage, two assumptions can be made: either the passive film has changed, or the oxido-reduction potential of the solution has modified toward more noble values. Notably, such behaviour has been observed in other works also [23, 30, 32] and is generally associated with the presence of radiolysis-induced radicals. The phenomenon can be described as follows: there is a rapid potential change (either toward oxidising or reducing values) at the beginning of irradiation followed by a steady state potential throughout the irradiation, and finally, after the stoppage of the irradiation, a transient phase is followed by a slower evolution toward a new potential.

The modifications that the medium undergoes during the irradiation is due to the production of free radicals [**31**]. Most radiolytic free radicals and excited species are created near the end of the proton range known as the Bragg peak. These free radicals are known to recombine with dissolved oxygen and lead to the formation of $H_2O_2$ [**22, 29**]. Consequently, the passive layer/solution interface remains in contact with the radical species ($H^{\bullet}$, $O^{\bullet}$, $OH^{\bullet}$, etc.) as well as the recombination products (e.g., $H_2O_2$). The red curve depicted in **Figure 8** shows the evolution of the corrosion potential during irradiation. This evolution follows the variations described in **Figure 7** during the irradiation beam application. The blue curve shows the evolution of the potential before irradiation when $H_2O_2$ is added after 7 min of immersion. The potential increases and reaches a value observed under irradiation, and the shapes of both the curves are similar.

The results presented in **Figure 8** present a powerful argument to prove the effect of the radiolysis in the solution on the corrosion potential evolution. Anodic polarisation curves were drawn to identify whether a change in passive behaviour could explain the potential ennoblement, as shown in **Figure 9**.

The anodic curve obtained for the 316L stainless steel sample in the sodium sulphate solution before irradiation (black curve) indicates a corrosion potential close to -280 mV/MSE and shows for more anodic potential that the electrochemical behaviour of the substrate is characterised by a passive state. The current density $i$ in the anodic portion is low (less than 10 µA/cm²), as also reported in [**34**]. The polarisation curve obtained for the sample under irradiation (red curve) exhibits a maximum corrosion potential of approximately 0 mV/MSE. In comparison with the curve plotted for the sample without irradiation, the difference between the corrosion potentials is approximately 280 mV. The same shift is observed when $H_2O_2$ is added to the neutral aerated sodium sulphate electrolyte. That confirms the importance of the modifications that the medium undergoes when under irradiation, which

involves modifications in the chemistry of the medium due to the formation of free radicals and then $H_2O_2$ observed previously by several authors, as Wang et al. [23] and more recently by Y. Wada et al. [**35**]. The potentials for which the reactions are involved correspond to the domain of existence of $Cr_2O_3$ growing. They are the same whatever the state of the medium: with or without irradiation, which indicates that the nature of the passive films remains the same. We assume that the film is made of oxy-hydroxide, mainly a mixture of $Cr_2O_3$ and $Cr(OH)_3$ as the inner layer and iron oxide and hydroxide as the outer layer, as it was previously identified by Z. Wang *et al.* [36]. This is obviously a global description, and the exact demarcation between each layer is difficult to identify.

If the potential ranges are identical, the current densities differ in the passive range, and are slightly higher under irradiation conditions. In general, when the current densities are higher, it is because more dissolution of the material is required to maintain the passive film and the barrier function of the passive film is less prominent. These observations were confirmed with experiments performed in a deaerated environment, as shown in **Figure 10**. The potentiodynamic curves exhibited an increase in both potential and current density in irradiation conditions. For reasons of clarity, the cathodic part of the polarisation curve under irradiation is not shown. The polarisation curve obtained for the stainless steel sample in an aerated solution is represented by the black curve. As demonstrated by the blue curve, obtained with the deaerated solution, the electrochemical behaviour of stainless steel shifts to a more cathodic domain due to oxygen removal, which is oxidising. The corrosion potential shifts toward cathodic values, driven by proton reduction. Under irradiation also, the trends are the same as described previously. The shift toward a nobler potential due to the radiolysis effect is represented by the red curve. Under irradiation, the dissolved oxygen removed performed by $N_2$ bubbling results in a slight shift of the corrosion towards cathodic values, and is represented by the green curve. It should be noted that it was not possible to remove

313 oxygen completely since it is continuously produced by water radiolysis. The higher current
314 density recorded in the cathodic part of the green curve is due to the production of higher
315 quantities of reducing species during irradiation. These curves provide information about the
316 reaction potential and its kinetics from the current densities. To understand the evolution of
317 the passive film and quantify some of its properties, electrochemical impedance
318 measurements were obtained.

319 Electrochemical impedance measurements were obtained before, during, and after the
320 irradiation. **Figure 11** shows the impedance (|Z|) and phases ($\varphi$) observed for these three
321 conditions. They were adjusted from the ohmic drop and are represented in Bode coordinates.
322 All impedance diagrams were characterised by two time constants. The time constant for the
323 low frequency range was not well defined in the result obtained during irradiation (blue
324 curve). The high-frequency part of the phase angle was defined by a plateau for a phase less
325 than -90°, which is attributed to the constant-phase-element response due to the presence of
326 the passive film. It should be underlined that in the impedance diagram, the plateau is not very
327 well defined, probably due to the difficulty in calculating the electrolyte resistance correctly.
328 Thus, the high-frequency time constant is attributed to the passive film response and the time
329 constant at the low frequency is attributed to the charge transfer at the passive film/electrolyte
330 interfaces. The impedance analysis performed in our study is based on the graphical method
331 reported in [37] and the CPE behaviour is analysed with the help of the power-law model,
332 largely employed to attribute a physical meaning to the CPE obtained for passive films [29].
333 The graphical or fitted parameters corresponding to the high-frequency time constants and the
334 corrosion potential values are reported in **Table 1**. The table shows that some values deviate
335 from the mean. These values are distributed over a range to provide information on the
336 dispersion of the results.

The potential values for the three irradiation conditions confirm the trends described above with a demonstrated ennoblement of potential related to the chemistry of the environment. This evolution may also explain the significant changes in the resistance of the electrolyte, which tends to decrease during and after irradiation. Moreover, this evolution cannot be attributed to corrosion phenomena because the material remains passive in all the cases. The dissolution of the material is insufficient for modifying the resistance of the electrolyte. Whatever the condition, the CPE parameter $\alpha$ remains close to 0.8, which is an intermediate value between a resistive (0.5) and an ideal capacitive (1) behaviour. The capacitance of the passive film is associated with that of the space charge and is graphically identified on a Cole-Cole diagram representing the imaginary part of the capacitance as a function of its real part, according to the relation:

$$C(\omega) = \frac{1}{j\omega(Z-R_e)} \qquad \text{Eq. 1}$$

As shown in the **Table 1**, the capacitance value decreases under irradiation and returns to a value close to its initial value after irradiation. The behaviour of the passive film can therefore be considered as reversible between the before and after irradiation periods.

From the space charge capacitance, it is possible to define the thickness of the passive film, as given by:

$$C_{sc} = \frac{A\varepsilon\varepsilon_0}{\delta_{sc}} \qquad \text{Eq. 2}$$

Here, $C_{sc}$ corresponds to the space charge capacitance, A to the exposed area, $\varepsilon$ to the permittivity of the passive film (12 for $Cr_2O_3$), $\varepsilon_0$ to the permittivity of the vacuum, and $\delta_{sc}$ to the thickness of the passive film. The film thickness was estimated at 6 nm before irradiation, 12 nm during irradiation, and 4 nm after irradiation. Therefore, the thickness variation seems reversible. The thinner the film, the more protective it is [**37, 38**]. It is possible that under irradiation, the passive film may be less protective since it is more defective.

The power-law model was specifically used for analysing the CPE behaviour in the high frequency ranges of the electrochemical impedance diagrams because it allows the evaluation of the resistivity distribution through the passive film [**39**]. This distribution is established by the equation:

$$Q = \frac{(\varepsilon\varepsilon_0)^{\alpha}}{g\delta\rho_{\delta}^{1-\alpha}} \qquad \text{Eq. 3}$$

Here, $g = 1 + 2.88\left(\frac{1}{1-\alpha}\right)^{-2.375}$, $\delta$ is the thickness of the passive film, and $\rho_{\delta}$ and $\rho_0$ are the resistivities at the passive film/electrolyte and 316L stainless steel/passive film interfaces, respectively.

The resistivity $\rho_{\delta}$ decreases significantly under irradiation (**Table 1**). $\rho_0$ is remains constant before and during irradiation, but increases by one order of magnitude after irradiation. **Figure 12** shows the resistivity distributions through the passives film for the three irradiation conditions, based on a dimensionless representation of the thickness (0 corresponds to the 316L/passive film interface ($\rho_0$ ) and 1 corresponds to the passive film/sodium sulphate solution interface ($\rho_{\delta}$ )). These results support the assumption made during the passive film analysis that a thicker film presents a weaker barrier. In our case, the metal oxide interface did not change before and during the irradiation. The polarisation curves indicated that the potentials were the same, which indicates the similar nature of the film. Thus, the oxide/solution interface is less resistive under irradiation either because of the more significant contribution of the hydroxide under irradiation (due to the presence of radiolytic species of the solution), or because of creation of defects in the passive film due the beam output. Further analyses are underway to identify the exact type of contribution. The argument leans more in favour of the formation of a more significant hydroxide because once the irradiation is interrupted, $\rho_0$ reaches the maximum value and $\rho_{\delta}$ is substantially similar to the initial value without irradiation. A higher resistivity at the metal/oxide interface

385 characterises a more significant passive film maturity in terms of the hydroxide/oxide ratio,
386 with more $Cr_2O_3$. It is therefore likely that the overvoltage applied to the system during
387 irradiation contributed to the promotion of deprotonation, as described in Okamoto's model
388 for passive film formation [**11**].

389 **3.2. Irradiation effect on the tribo-electrochemical behaviour of 316L**

390 Friction tests were conducted after immersion during 14h. This period insure a reproducibility
391 of the passive state. **Figure 13.a** shows the changes in potential during friction and **Figure**
392 **13.b** shows the changes in the current. At time t = 0, the potential was equal to the potential of
393 the passivated material without friction. When friction was applied, the potential dropped
394 significantly to a value close to -0.3 VvsMSE, and remained stable throughout the friction
395 experiment. The potential value did not change when the irradiation beam was applied. The
396 figure shows the corresponding curve in red. When the friction was interrupted, the potential
397 increased to a value close to 0 VvsMSE.
398 In **Figure 13.b**, the changes in the current indicate that the current is almost zero without
399 friction and corresponds to a value required for the maintenance of the passive film. When
400 friction was applied, there was a significant increase in the current that indicated the
401 activation of the surface, as shown in the figure. Thereafter, the current decreased to a stable
402 value (from 0 s to 500 s). The current density is the result of the competition between the
403 depassivation of the sample subjected to friction and the repassivation. The black curve in the
404 figure corresponds to measurements recorded before radiation. The red curve indicates the
405 behaviour under irradiation. In the figure, no significant difference in behaviour is seen
406 between the presence or absence of irradiation.

407 **Figure 14** presents a focused view of the potential and current transients. Both the current and
408 potential transients reflect the passivation and depassivation phenomena. When the current

increases, the passive film under the friction-inducing pin is destroyed. When the movement of the pin is suspended, the current decreases, and the wear track is repassivated.

The transients can be analysed on the basis of the work of Keddam et al. [**40**], in which the repassivation phenomenon was adjusted according to two time constants. The first is attributed to the species adsorption phenomena, prior to the reconstruction of the passive film. This phenomenon is associated with the formation of a 2D layer on the wear track, as shown in **Figure 15**. The second time constant corresponds to the 3D phenomenon associated with the passive film growth.

The relationships proposed by Keddam et al. can be written as [40]:

$$I = I_1 e^{-t/\tau_1} + I_2 e^{-t/\tau_2} \qquad \text{Eq. 4}$$

Here, $I_1$ and $I_2$ correspond to the two components of current which contribute to the fit of current fall and $\tau_1$ and $\tau_2$ correspond to the adsorption time constants of the 2D layer and the growth of the 3D film, respectively. These parameter have been introduced by Beck [41] and illustrated by Dalbert et al [42].

The constant $\tau_1$ was successfully analysed in this study; however, $\tau_2$ could not be analysed in this preliminary study, probably because the repassivation time was insufficient to allow the stable growth of the passive film. **Figure 16** shows the evolution of the adsorption time constant of the species prior to repassivation under different conditions. The red curve indicates a time constant value of 0.3 s under friction without irradiation. When irradiation is applied after 800 current transients, the time constant (red curve) drops drastically to 0.25 s. The time constant then decreases, implying a faster adsorption step. The black curve confirms this decrease in the time constant for the irradiation applied before the pin was moved. The time constant remains 0.25 throughout the transients. In an attempt to confirm the representativeness of the effects of the $H_2O_2$ produced by radiolysis mentioned in the first part

433 of this work, friction tests were performed, with $H_2O_2$ added after 1250 transients. After this
434 addition (blue curve), the time constant dropped significantly under the effect of radiation.
435 The extent of this decrease varied for different $H_2O_2$ concentrations. Work is still in the
436 progress to confirm this observation.

437 **3. Conclusions**

438 The objective of this study was to develop an experiment to characterise the behaviour of a
439 316L stainless steel sample subjected to tribocorrosion under irradiation. Such an experiment
440 required a tribocorrosimeter design that could be installed on the cyclotron of the CEMHTI
441 laboratory to allow *in situ* proton irradiation. This original design enabled us to perform
442 superficial mechanical stresses on the stainless steel while recording the electrochemical
443 measurements.

444 The obtained measurements indicated a significant increase in the corrosion potential during
445 irradiation. Experiments by adding hydrogen peroxide to the solution in the absence of
446 irradiation demonstrated that this potential evolution was mainly caused by a change in the
447 oxidative power of the solution due to the presence of radiolytic species in the solution. Of
448 course this experiment simulates the effects of radiolysis without taking into account the
449 defects created in the passive film by the irradiation beam. The time scale investigations
450 performed in this work indicated that the characteristics of the passive film remained identical
451 before and after the application of irradiation. The PLM was used to obtain the impedance
452 measurement parameters. The results showed a thickening of the passive film during
453 irradiation, with the other parameters remaining unchanged. These are preliminary results that
454 do not correspond to those obtained by other authors for longer irradiations under more
455 representative nuclear conditions. More detailed studies will be envisaged in the near future to
456 complement the thickness measurements with other techniques.

The resistivity of the passive film at the steel/oxide interface remained the same before and after the irradiation. The oxide/solution resistivity dropped significantly during irradiation. Further analyses are being considered to identify whether this is an effect of the solution caused by the production of more hydroxide at the oxide solution interface due to the presence of $H_2O_2$ or an effect of the presence of irradiation defects at the interface, which may have promoted the formation of a degraded passive film structure. Considering the changes in the oxidising power of the solution, the various phenomena involved during tribocorrosion were studied. This preliminary work was based on the study of repassivation time constants after depassivation under friction, and it was observed that adsorption, a preliminary step before the growth of the passive film, was faster under irradiation. At this point, the growth stage could not be characterised fully. As a final observation, the behaviour of the passive film under the irradiation was found to be reversible.

**Acknowledgements**

This project received financial support from the CNRS through the NEEDS program and, more recently, through the MITI interdisciplinary programs. The authors also thank P. Sireira, C. Déhée, A. Guichon, and C. Panetier for their fruitful contributions during their Master Project and O. Farid from Nuclear Research Center, Cairo, Egypt during his scientist internship at MATEIS UMR 5510 CNRS, INSA Lyon.

# 4. References

[1] P. M. Scott, P. Combrade, General corrosion and stress corrosion cracking of Alloy 600 in light water reactor primary coolants, Journal of Nuclear Materials 524 (2019) 340-375. https://doi.org/10.1016/j.jnucmat.2019.04.023.

[2] P. L. Andresen, A brief history of environmental cracking in hot water, Corrosion 75, 3 (2019) 240-253. https://doi.org/10.5006/2881

[3] S. K. Dwivedi, M. Vishwakarma, Hydrogen embrittlement in different materials: A review, International Journal of Hydrogen Energy 43, 46 (2018) 21603-21616. https://doi.org/10.1016/j.ijhydene.2018.09.201.

[4] D. Hertz, Approach to analysis of wear mechanisms in the case of RCCAs and CRDM latch arms: From observation to understanding, Wear 261 (2006) 1024–1031. https:// doi:10.1016/j.wear.2006.03.037

[5] P. Ponthiaux, J.-P. Celis, F. Wenger, Tribocorrosion: a new approach of the problems related to combined friction and wear in a corrosive surrounding, Matériaux et Techniques 99, 1 (2011) 2-4.

[6] W.–J. Chitty, C. Falcand, Tribocorrosion in Pressurized Water Reactors, 3rd International Symposium on Tribo-Corrosion: Research, Testing, and Applications; Atlanta; United States; 19-20 April 2012; Code 112802 GA, in ASTM Special Technical Publication, West Conshohocken, PA 2012. Vol. STP 1563, January, (2013) 125-138 https://doi.org./10.1520/STP156320120040.

[7] B. Normand, A. Pierre, J. Pagetti, Electrochemical and surface studies of the passive layers grown on sputter-deposited nitrogen-stainless steel alloys in 1M $H_2SO_4$ solution, Corrosion Science 37, 10 (1995) 1537-1549. https:// 10.1016/0010-938X(95)00045-L.

[8] D. Landolt, Electrochemical and materials aspects of tribocorrosion systems, Journal of Physics D: Applied Physics 39, 15 (2006) S01, 3121-3127. https:// 10.1088/0022-3727/39/15/S01.

[9] A. López-Ortega, J. L. Arana, R. Bayón, Tribocorrosion of passive materials: A review on test procedures and standards 2018, International Journal of Corrosion, Hindawi. ID 7345346. https://doi.org/10.1155/2018/7345346

[10] S. Cao, S. Mischler, Modeling tribocorrosion of passive metals – A review, Current Opinion in Solid State & Materials Science 22 (2018) 127–141. https://doi.org/10.1016/j.cossms.2018.06.001

[11] N. Sato, An overview on the passivity of metals, Corrosion Science, 31 (1990) 1-19. https:// 10.1016/0010-938X(90)90086-K

[12] G. S. Frankel, B. M. Rush, C. V. Jahnes, C. E. Farrell, A. J. Davenport and H. S. Isaacs, Repassivation Transients Measured with Thin Film Breaking Electrodes, Journal of The Electrochemical Society, 138, 2 (1991) 643-644.

[13] M. Itagaki, R. Oltra, B. Vuillemin, M. Keddam and H. Takenouti, Quantitative Analysis of Iron Dissolution during Repassivation of Freshly Generated Metallic Surfaces, Journal of The Electrochemical Society, 144 (1997) 1, 64-72. https://doi. 10.1149/1.1837366

[14] I. Chunga, M. Leeb, An experimental study on fretting wear behavior of cross-contacting Inconel 690 tubes, Nuclear Engineering and Design 241 (2011) 4103–4110. https://doi:10.1016/j.nucengdes.2011.08.024

[15] M. Laribi, A.B. Vannes, D. Tréheux, Study of mechanical behavior of molybdenum coating using sliding wear and impact tests, Wear 262 (2007) 1330–1336. https:// doi:10.1016/j.wear.2007.01.018

[16] P. Scott, A review of irradiation assisted stress corrosion cracking, Journal of Nuclear Materials 211(1994) pp. 101-122. https;//doi: 10.1016/0022-3115(94)90360-3

[17] T. Shoji, S.I. Suzuki, V. S. Raja, Current status and future of IASCC research, Journal of Nuclear Materials, 258-263 (1998) 241–251. https://doi: 10.1016/S0022-3115(98)00304-3

[18] S.M. Bruemmer, E. P. Simonen, P. M. Scott, P. L. Andresen, G. S. Was, J. L. Nelson, Radiation-induced material changes and susceptibility to intergranular failure of light-water-reactor core internals, Journal of Nuclear Materials 274 (1999) 299-314. https://doi: 10.1016/S0022-3115(99)00075-6

[19] S.M. Bruemmer, D.J Edwards, V.Y. Gertsman, E.P. Simonen, Grain boundary modification during neutron irradiation at intermediate temperatures, In Proc. 10th Int. Symp. on Environmental Degradation of Materials in Nuclear Power System - Water Reactors, Materials Research Society Symposium - Proceedings 650, no. 0008V, (2001) R2.1.1-R2.1.12 2001.

[20] S. S. Raiman, D. M. Bartels, G. S. Was, Radiolysis driven changes to oxide stability during irradiationcorrosion of 316L stainless steel in high temperature water, Journal of Nuclear Materials 493 (2017) 40-52. http://dx.doi.org/10.1016/j.jnucmat.2017.05.042

[21] S. S. Raiman, G. S. Was, Accelerated corrosion and oxide dissolution in 316L stainless steel irradiated in situ in high temperature water, Journal of Nuclear Materials 493 (2017) 207-218. http://dx.doi.org/10.1016/j.jnucmat.2017.05.043

[22] S. Le Caër, Water Radiolysis: Influence of Oxide Surfaces on $H_2$ Production under Ionizing Radiation, Water 2011, 3, 235-253. https://doi: 10.3390/w3010235

[23] M. Wang, S. Perrin, C. Corbel, D. Féron, Electrochemical behaviour of 316L stainless steel exposed to representative chemistry in pressurised water reactors under proton radiation, Journal of Electroanalytical Chemistry 737 (2015) 141–149. https://doi: 10.1016/j.jelechem.2014.10.015

[24] Shreir's corrosion, Fourth Ed., Corrosion in Radiolysis Induced Environments, Ed. By B. Cottis, M. Graham, R. Lindsay, S. Lyon, T.Richardson, D. Scantlebury, H. Stott, Pub. in G. O. H. Whillock, Vol 1 (2010), p. 89.

[25] G.S Was, Y. Ashida, P.L Andresen, Irradiation-assisted stress corrosion cracking, Corrosion Reviews 29 (2011) 1-2, 7–49. https://doi:10.1515/correv.2011.020.

[26] A. Ouerd, C. Alemany-Dumont, G. Berthomé, B. Normand, and S. Szunerits, Reactivity of titanium in physiological medium, Journal of Electrochemical Society 154 (2007) 10, C593-C601. https://doi: 10.1149/1.2769819.

[27] B. Hirschorn, M.E. Orazem, B. Tribollet, V. Vivier, I. Frateur, M. Musiani, J. Electrochem. Soc. 157 (2010) C452. https://doi:10.1149/1.3499564.

[28] B. Hirschorn, M.E. Orazem, B. Tribollet, V. Vivier, I. Frateur, M. Musiani, J. Electrochem. Soc. 157 (2010) C458. https://doi:10.1149/1.3499565.

560 [29] M.E. Orazem, I. Frateur, B. Tribollet, V. Vivier, S. Marcelin, N. Pébère, A.L. Bunge,
561 E.A. White, D.P. Riemer, M. Musiani, Dielectric properties of material showing
562 Constant-Phase-Element (CPE) impedance response, Journal of the Electrochemical
563 Society, 160 (2013) C215-C225. https://doi:10.1149/2.033306jes.

564 [30] B. Tribollet, V. Vivier, M.E. Orazem, EIS Technique in Passivity Studies:
565 Determination of the Dielectric Properties of Passive Films, EIS Technics,
566 Encyclopedia of electrochemistry, 2017. https://doi:10.1016/B978-0-12-409547-2.13817-X.

567 [31] J. F. Ziegler, M.D. Ziegler, J.P. Biersack, SRIM – The stopping and range of ions in matter
568 (2010). Nuclear Instruments and Methods in Physics Research Section B: Beam Interactions
569 with Materials and Atoms 268, 11–12 (2010) 1818-1823,
570 https://doi.org/10.1016/j.nimb.2010.02.091

571 [32] B. Muzeau, S. Perrin, C. Corbel, D. Simon, D. Ferron, Electrochemical behaviour of
572 stainless steel in PWR primary coolant conditions: Effects of radiolysis, Journal of
573 Nuclear Materials 419 (2011) 241–247. https:// doi:10.1016/j.jnucmat.2011.08.051.

574 [33] E. Leoni, C. Corbel,V. Cobut , D. Simond, D. Féron , M. Roya, O. Raquet,
575 Electrochemical behaviour of gold and stainless steel under proton irradiation and active
576 RedOx couples, Electrochimica Acta 53 (2007) 495–510. https://
577 doi:10.1016/j.electacta.2007.07.029.

578 [34] G. Tranchida, M. Clesi, F. Di Franco, F. Di Quarto, M. Santamaria, Electronic
579 properties and corrosion resistance of passive films on austenitic and duplex stainless
580 steels, Electrochimica Acta 273 (2018) 412-423.
581 https://doi.org/10.1016/j.electacta.2018.04.058

582 [35] Y. Wada, Y. Kani, K. Ishida, N. Ota, M. Ueno 55 (2018) 12, Radiolytic hydrogen
583 evolution in a closed vessel, Journal of Nuclear Science and Technology, 55 (2018) 12,
584 1481-1489. https://doi: 10.1080/00223131.2018.1519466

585 [36] Z. Wang, A. Seyeux, S. Zanna, V. Maurice, P. Marcus, Chloride-induced alterations of
586 the passive film on 316L stainless steel and blocking effect of pre-passivation,
587 Electrochimica Acta 329 (2020) 135159.

588 [37] N. Sato, An overview on the passivity of metals, Corrosion Science, Vol 31 (1990), pp.
589 1-19.

590 [38] S. Matsuda, T. Kikuchi, K. Sugimoto, Corrosion Science, Vol 31 (1990), pp. 161-166.

591 [39] S. Marcelin, B. Ter-Ovanessian, B. Normand, Electronic properties of passive films
592 from the multi-frequency Mott–Schottky and power-law coupled approach,
593 Electrochemistry Communications 66 (2016) 62–65.
594 http://dx.doi.org/10.1016/j.elecom.2016.03.003

595 [40] M. Keddam, F. Liao, P. Ponthiaux, V. Vivier, New advances in triboelectrochemistry:
596 from steady stateto impedance of abraded stainless steel in acidic medium, J Solid State
597 Electrochem 19 (2015) 2591–2599. https:// doi. 10.1007/s10008-015-2914-8.

598 [41] T. R. Beck, Electrochemistry of freshly-generated titanium surfaces—II. Rapid fracture
599 experiments, Electrochimica Acta. 1973;18:815–27. https://doi.org/ 10.1016/0013-
600 4686(73)85033-9.

601 [42] V. Dalbert, N. Mary, B. Normand, C. Verdu, S. Saedlou, In situ determinations of the
602 wear surfaces, volumes and kinetics of repassivation: Contribution in the understanding
603 of the tribocorrosion behaviour of a ferritic stainless steel in various pH, Tribology
604 International 150 (2020) 106374, https://doi.org/10.1016/j.triboint.2020.106374
605

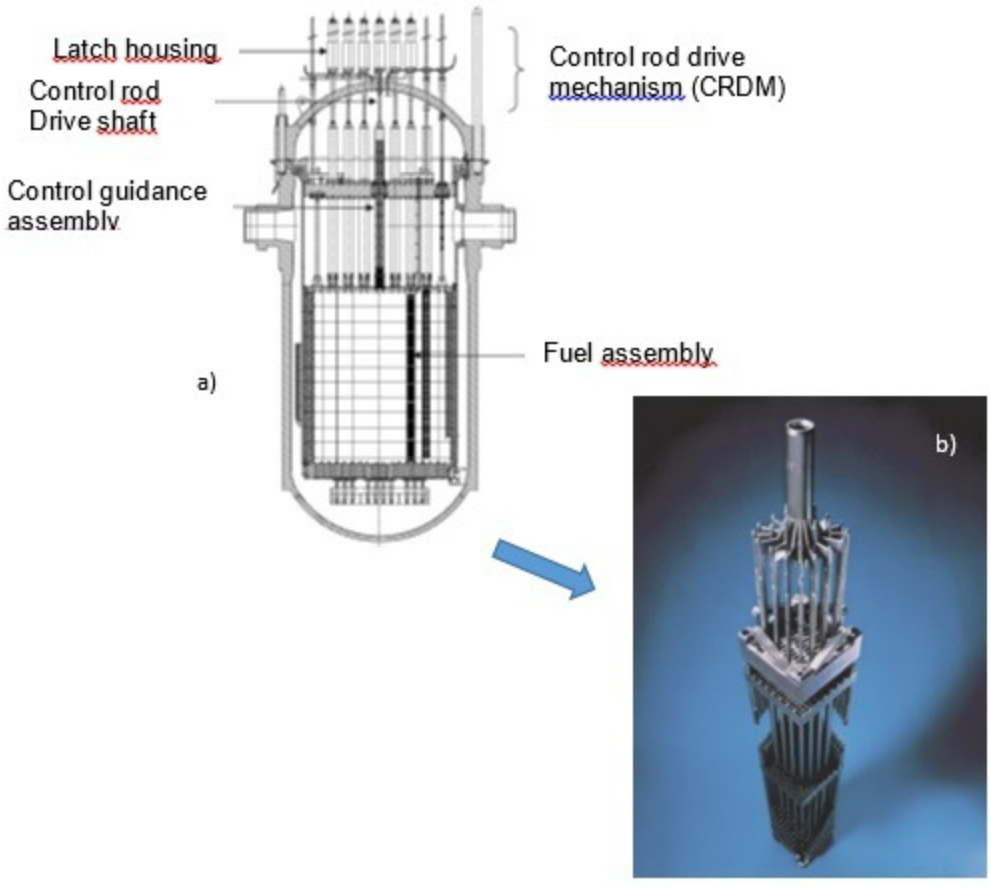
Latch housing
Control rod
Drive shaft
Control guidance
assembly
Control rod drive
mechanism (CRDM)
Fuel assembly
a)
b)

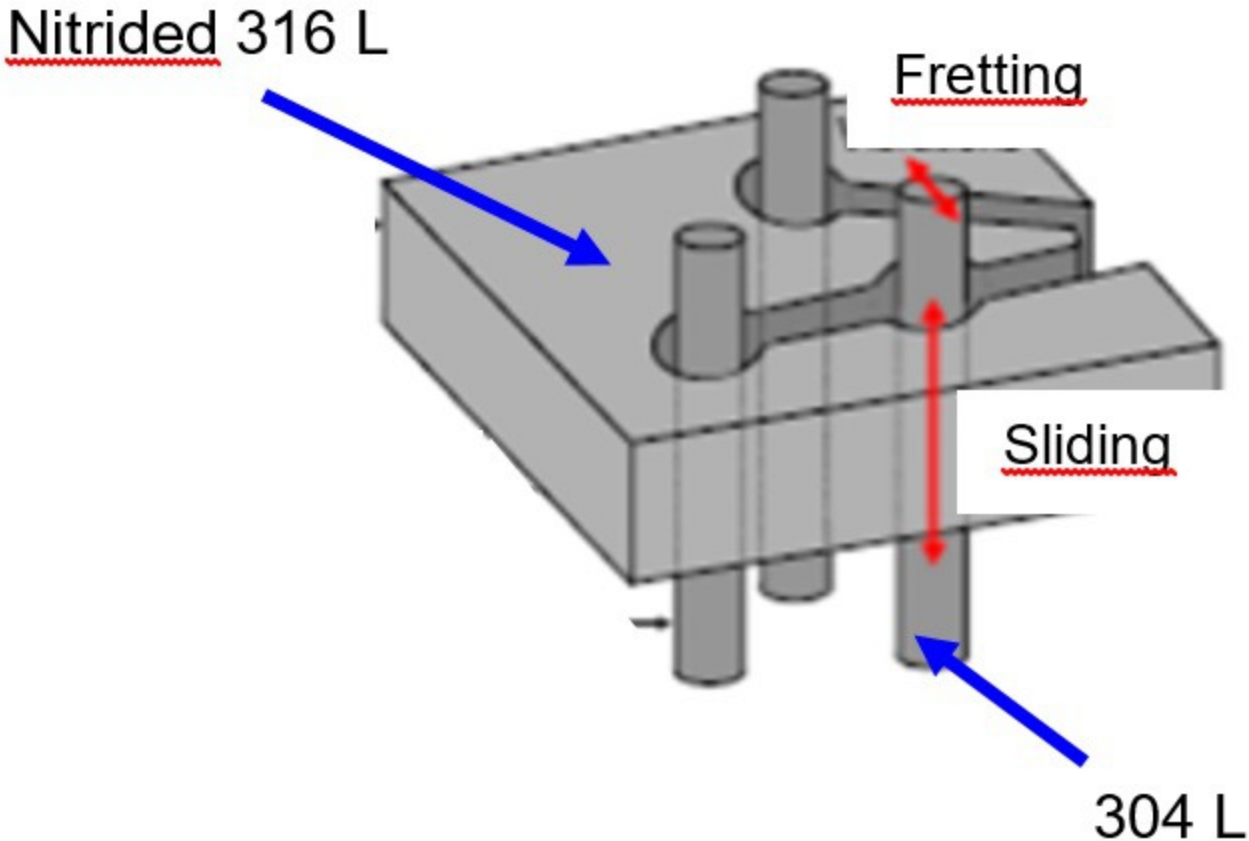
Nitrided 316 L
Fretting
Sliding
304 L

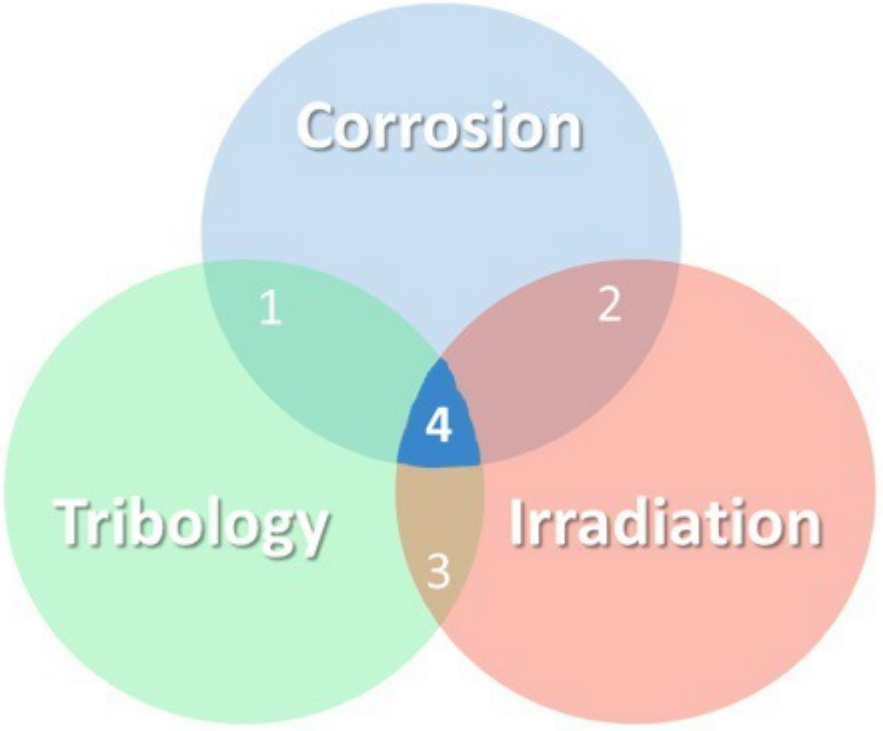


1 – Tribocorrosion
2 - Corrosion under irradiation
3 - Tribology under irradiation
4 - **Tribocorrosion under irradiation**

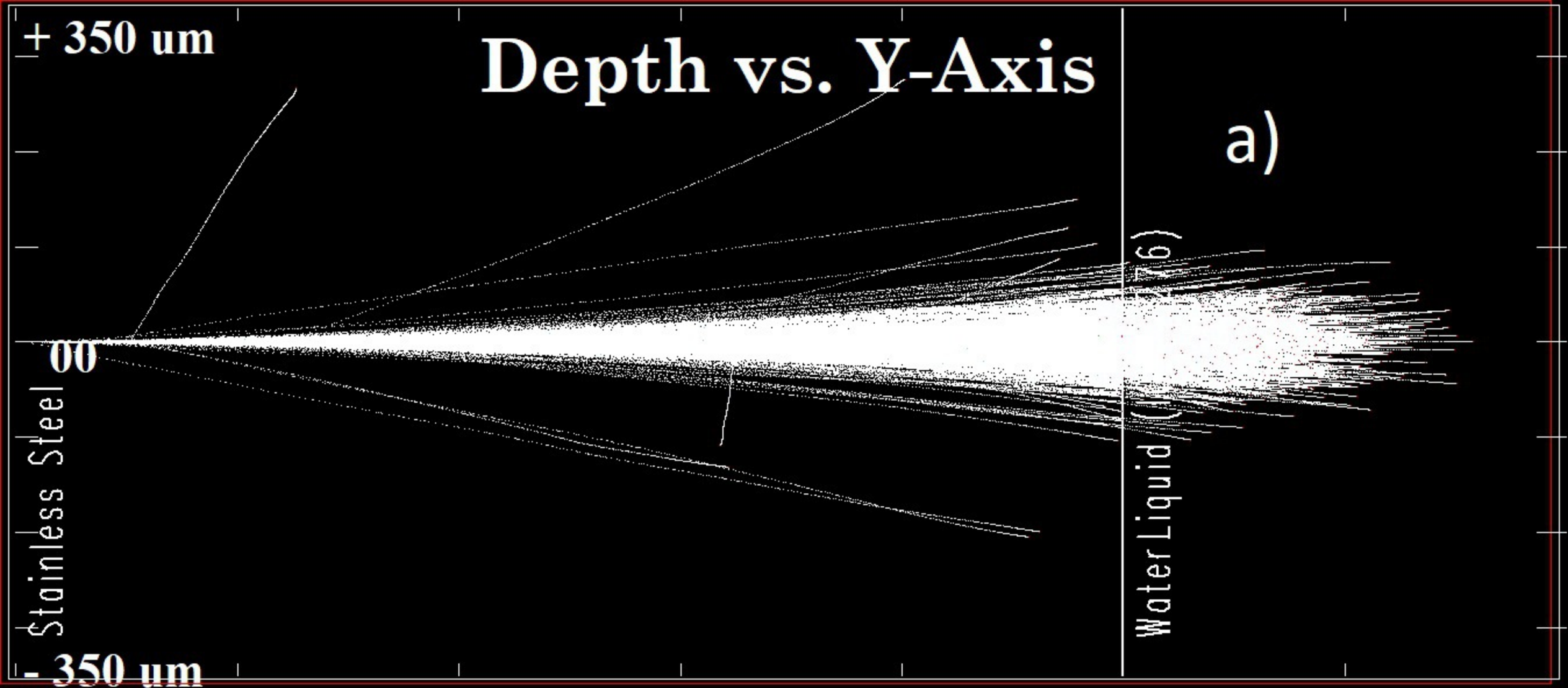
Depth vs. Y-Axis
+ 350 um
00
- 350 um
Stainless Steel
Water Liquid (
a)
0 A
-- Target Depth --
700 um

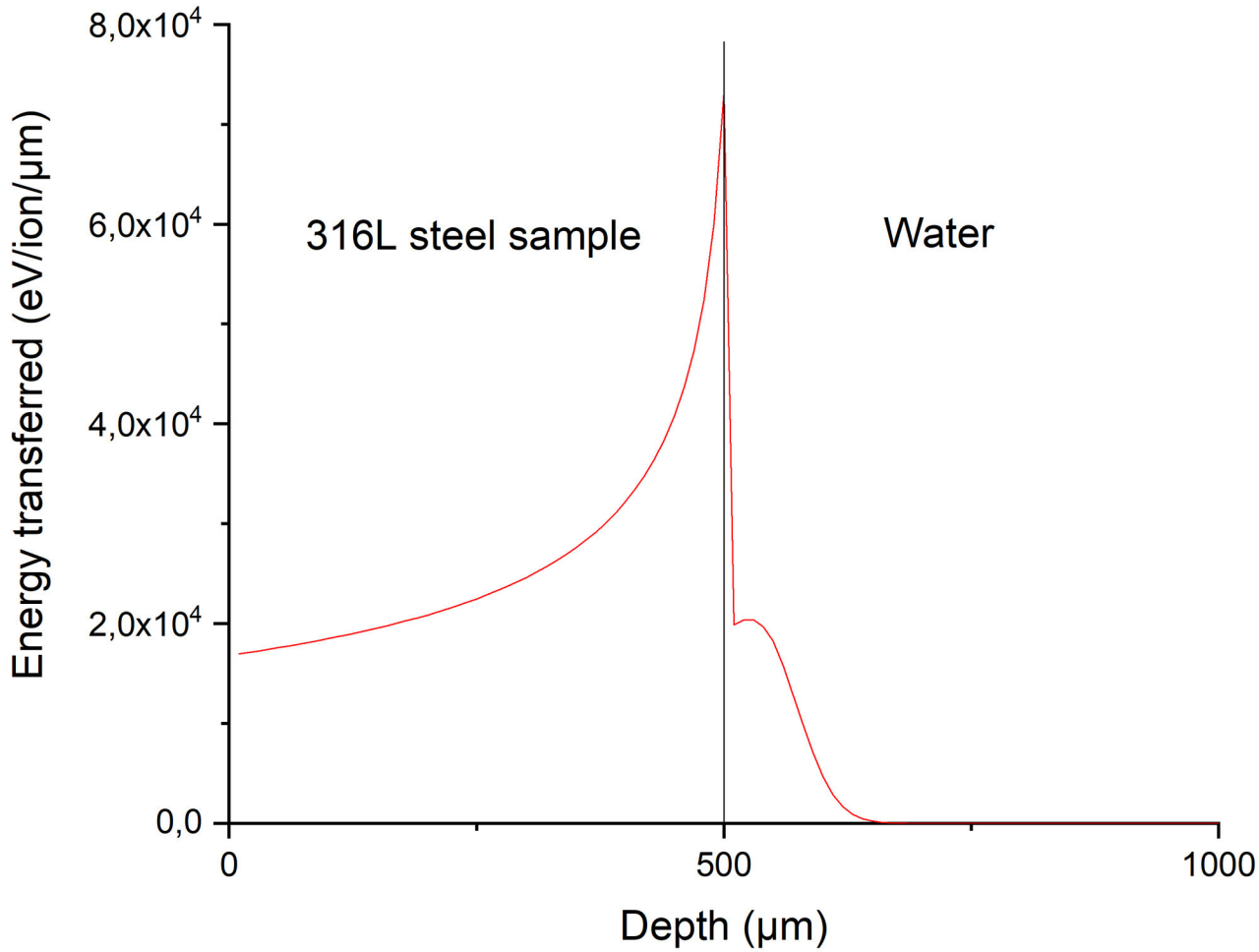
8,0x10^4
6,0x10^4
4,0x10^4
2,0x10^4
0,0
Energy transferred (eV/ion/µm)
316L steel sample
Water
0
500
1000
Depth (µm)

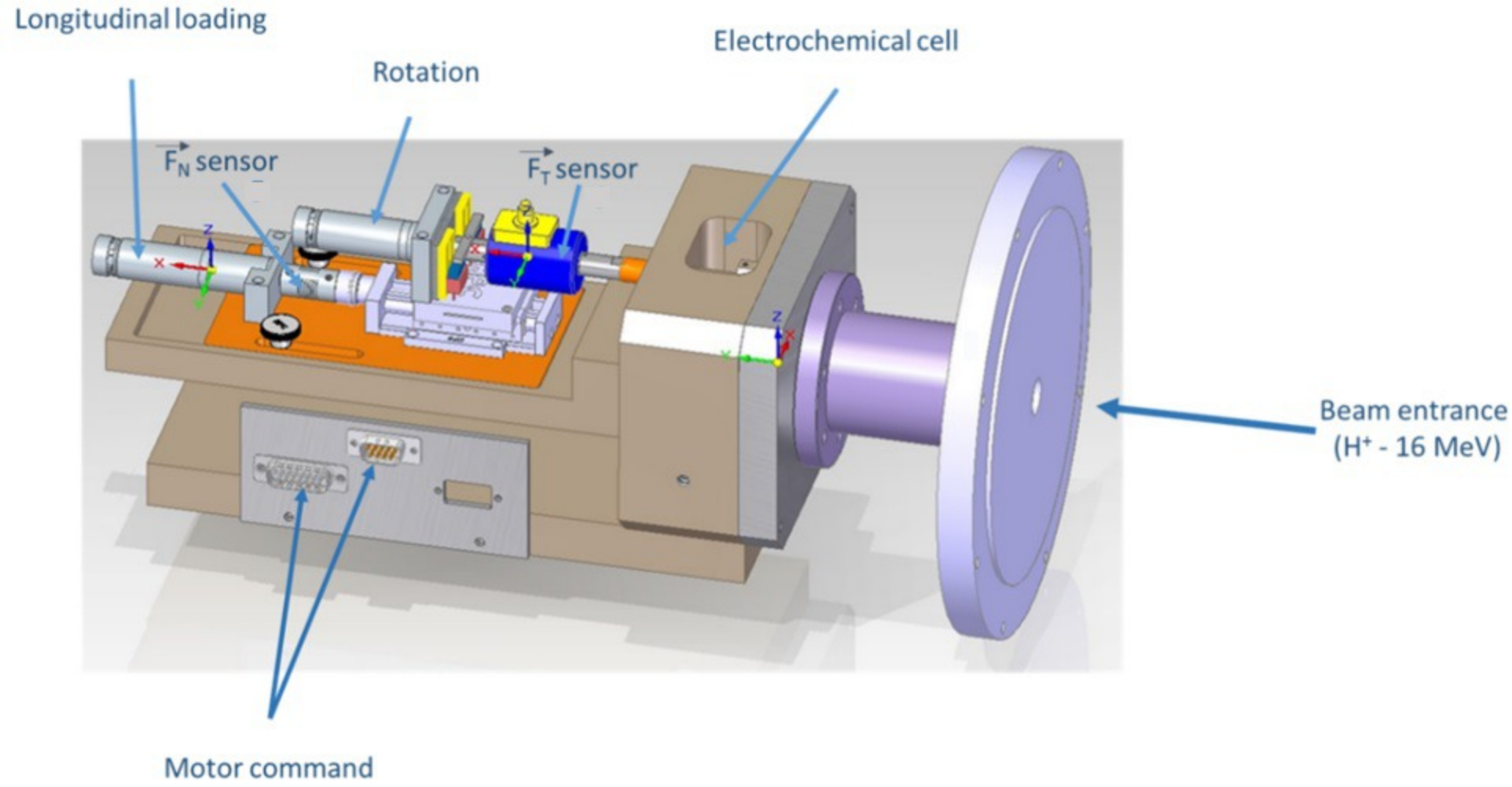
Longitudinal loading
Rotation
Electrochemical cell
$\overrightarrow{F_N}$ sensor
$\overrightarrow{F_T}$ sensor
Beam entrance
($H^+$ - 16 MeV)
Motor command

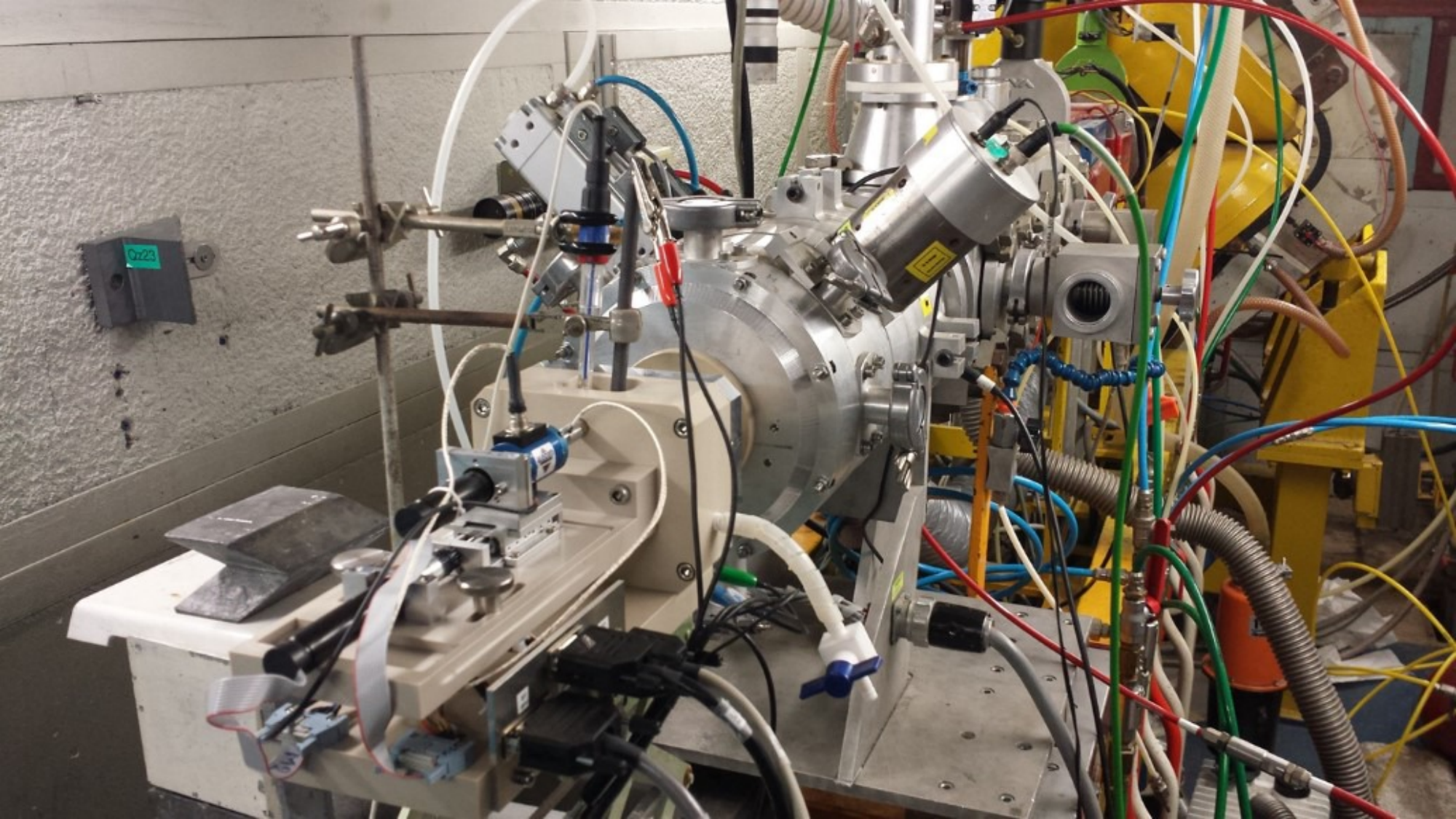
Qx23

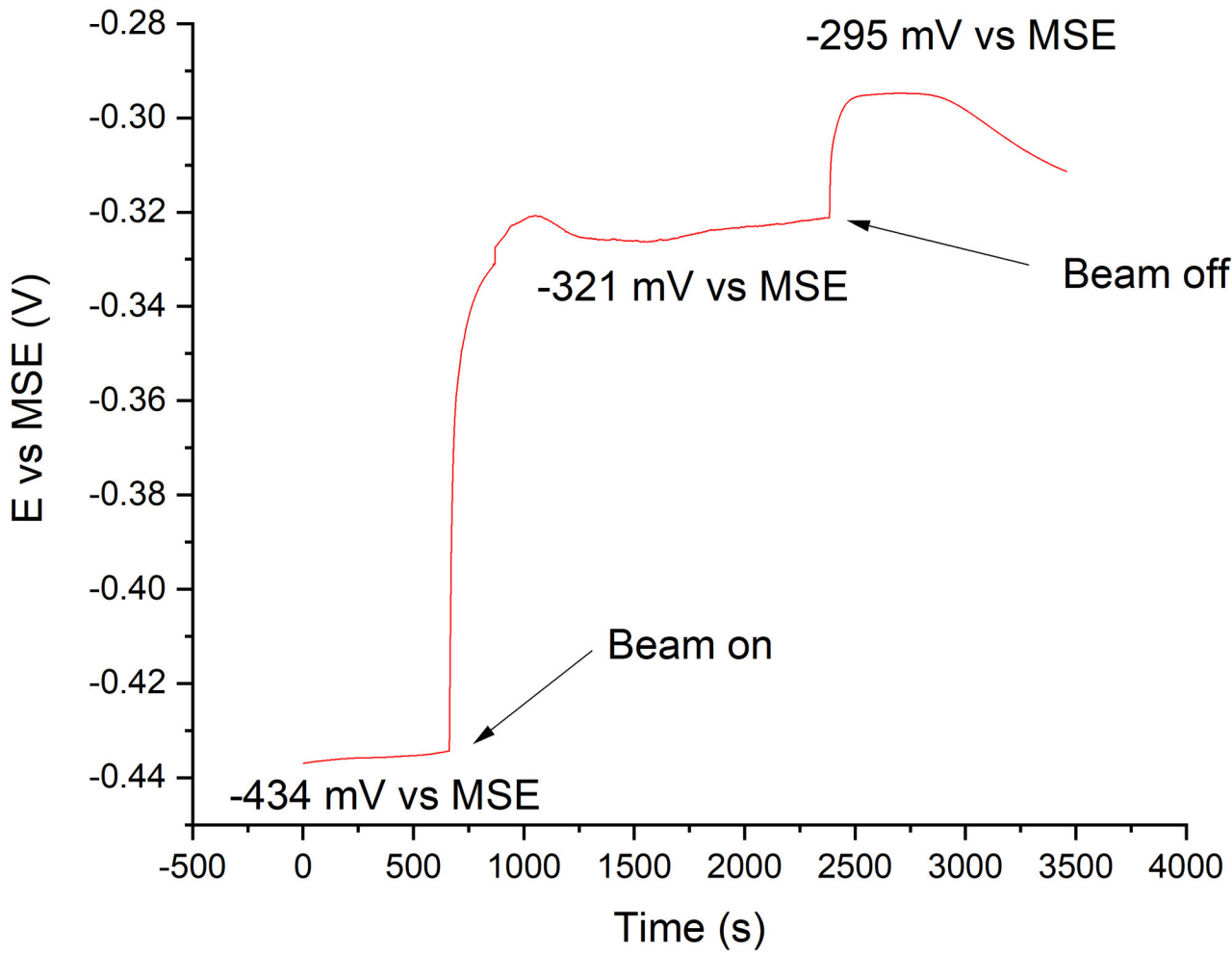
-0.28
-0.30
-0.32
-0.34
-0.36
-0.38
-0.40
-0.42
-0.44
E vs MSE (V)
-500
0
500
1000
1500
2000
2500
3000
3500
4000
Time (s)
-295 mV vs MSE
-321 mV vs MSE
-434 mV vs MSE
Beam off
Beam on

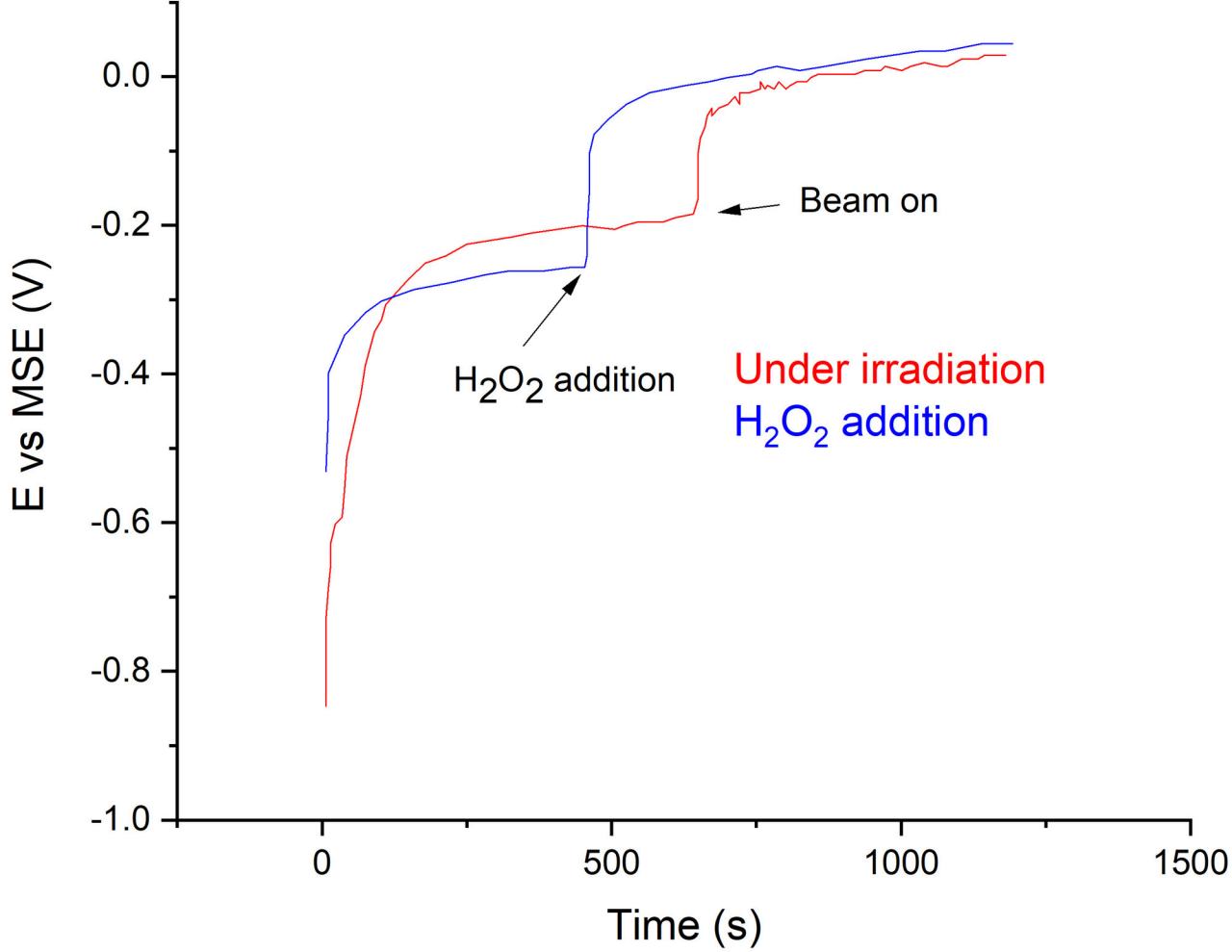
0.0
-0.2
-0.4
-0.6
-0.8
-1.0
E vs MSE (V)
0
500
1000
1500
Time (s)
Beam on
H2O2 addition
Under irradiation
H2O2 addition

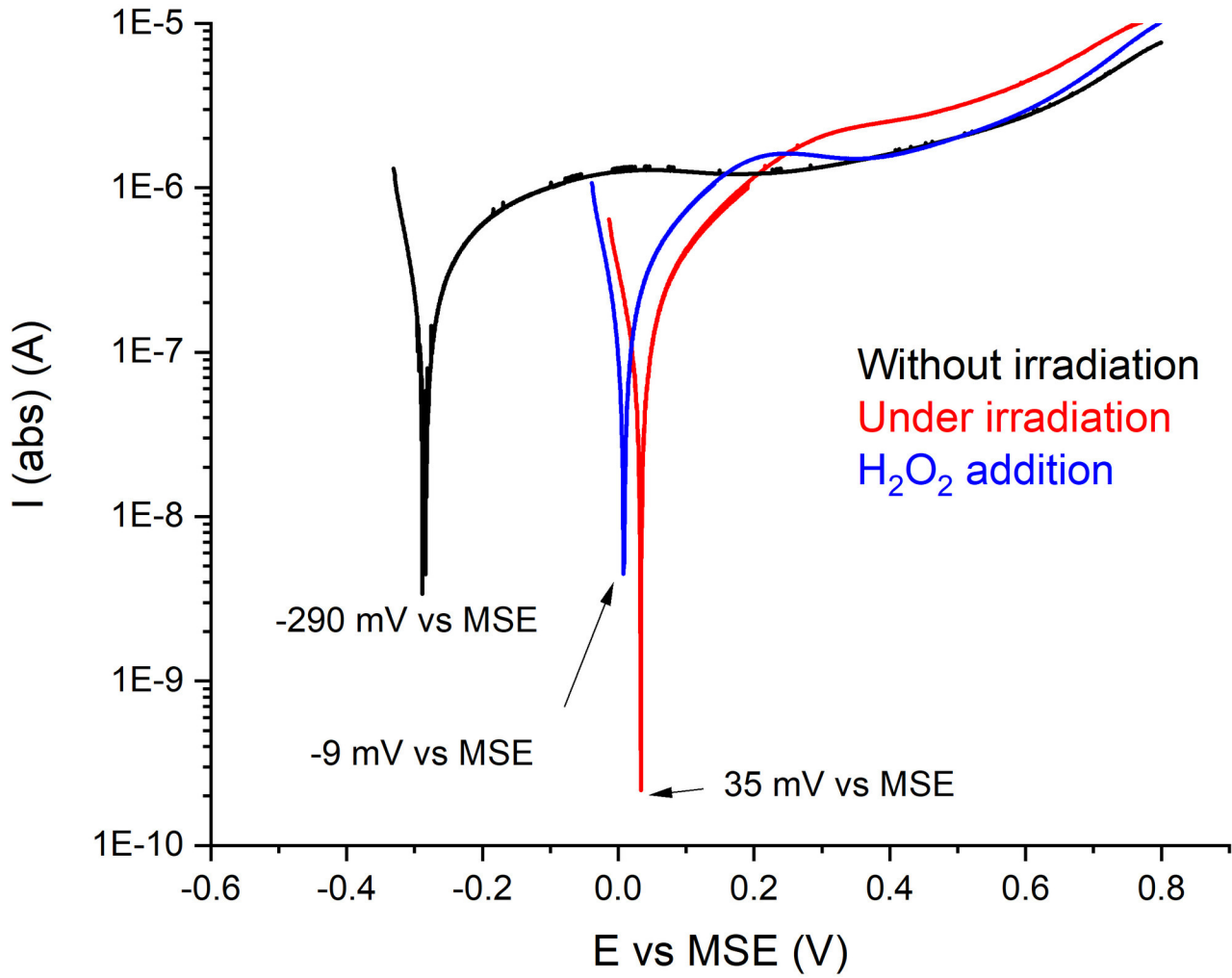
1E-5
1E-6
1E-7
1E-8
1E-9
1E-10
I (abs) (A)
-0.6
-0.4
-0.2
0.0
0.2
0.4
0.6
0.8
E vs MSE (V)
Without irradiation
Under irradiation
H2O2 addition
-290 mV vs MSE
-9 mV vs MSE
35 mV vs MSE

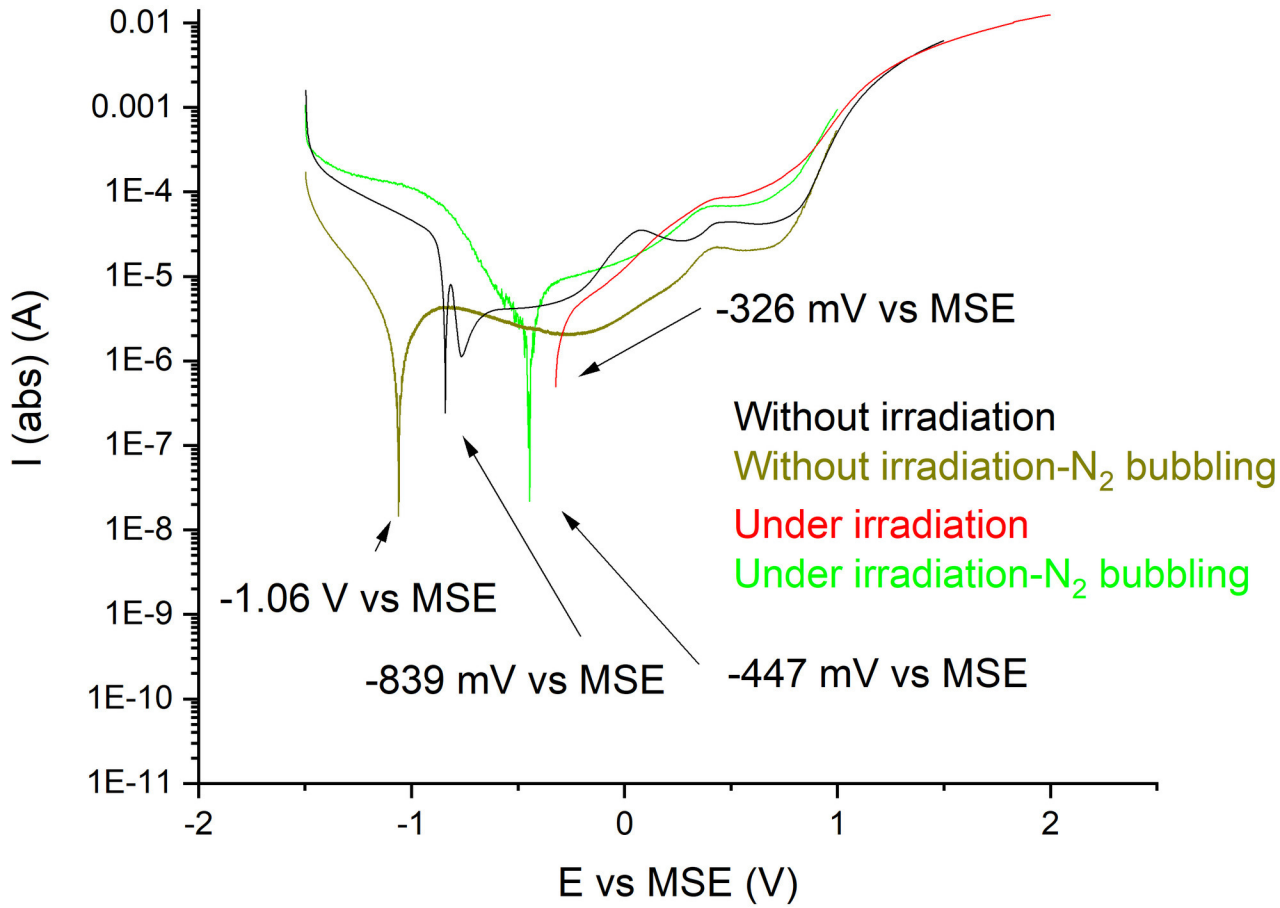
0.01
0.001
1E-4
1E-5
1E-6
1E-7
1E-8
1E-9
1E-10
1E-11
I (abs) (A)
-2
-1
0
1
2
E vs MSE (V)
-326 mV vs MSE
Without irradiation
Without irradiation-N2 bubbling
Under irradiation
Under irradiation-N2 bubbling
-1.06 V vs MSE
-839 mV vs MSE
-447 mV vs MSE

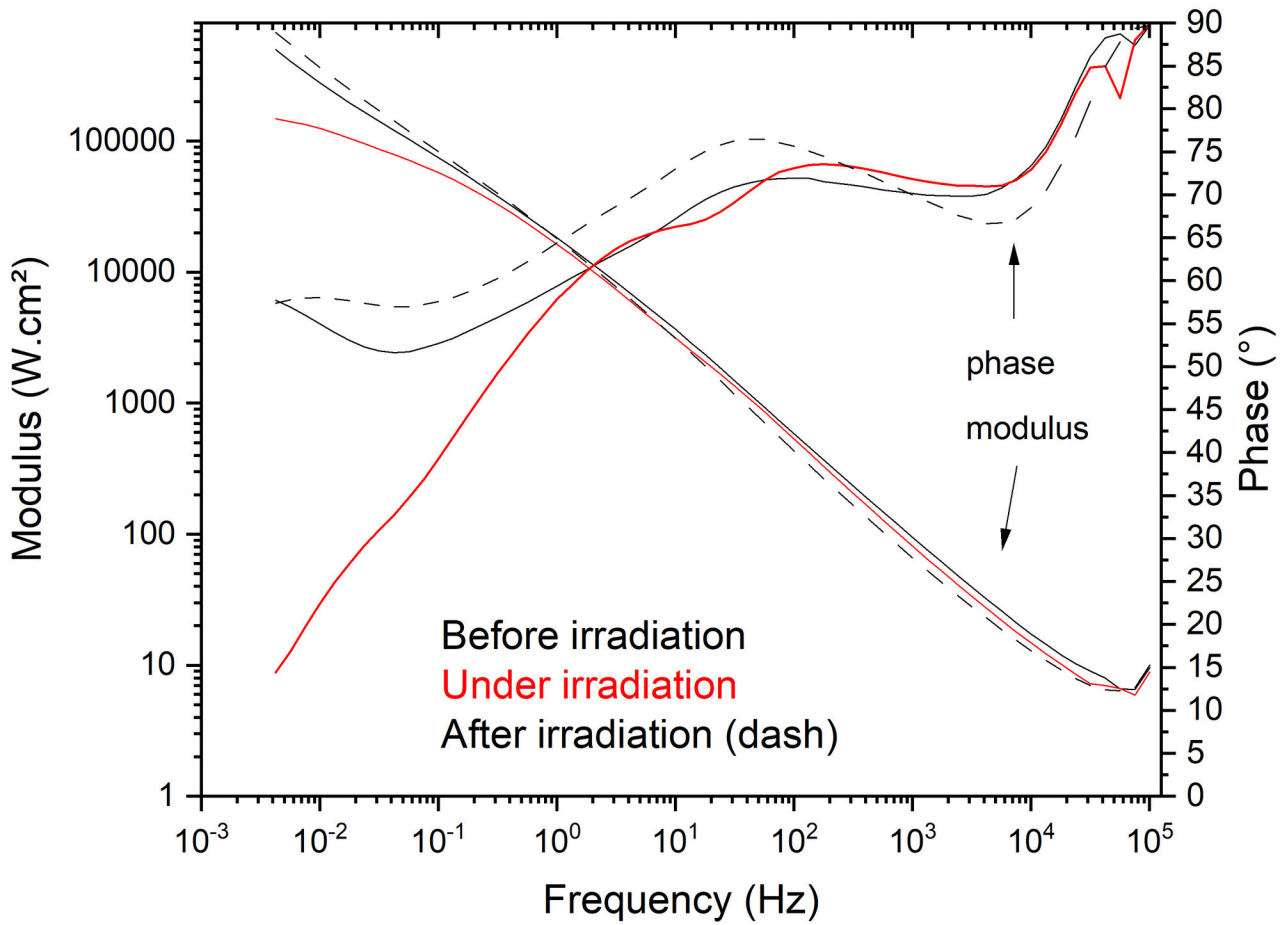
Modulus (W.cm²)
Phase (°)
Frequency (Hz)
100000
10000
1000
100
10
1
90
85
80
75
70
65
60
55
50
45
40
35
30
25
20
15
10
5
0
10⁻³
10⁻²
10⁻¹
10⁰
10¹
10²
10³
10⁴
10⁵
phase
modulus
Before irradiation
Under irradiation
After irradiation (dash)

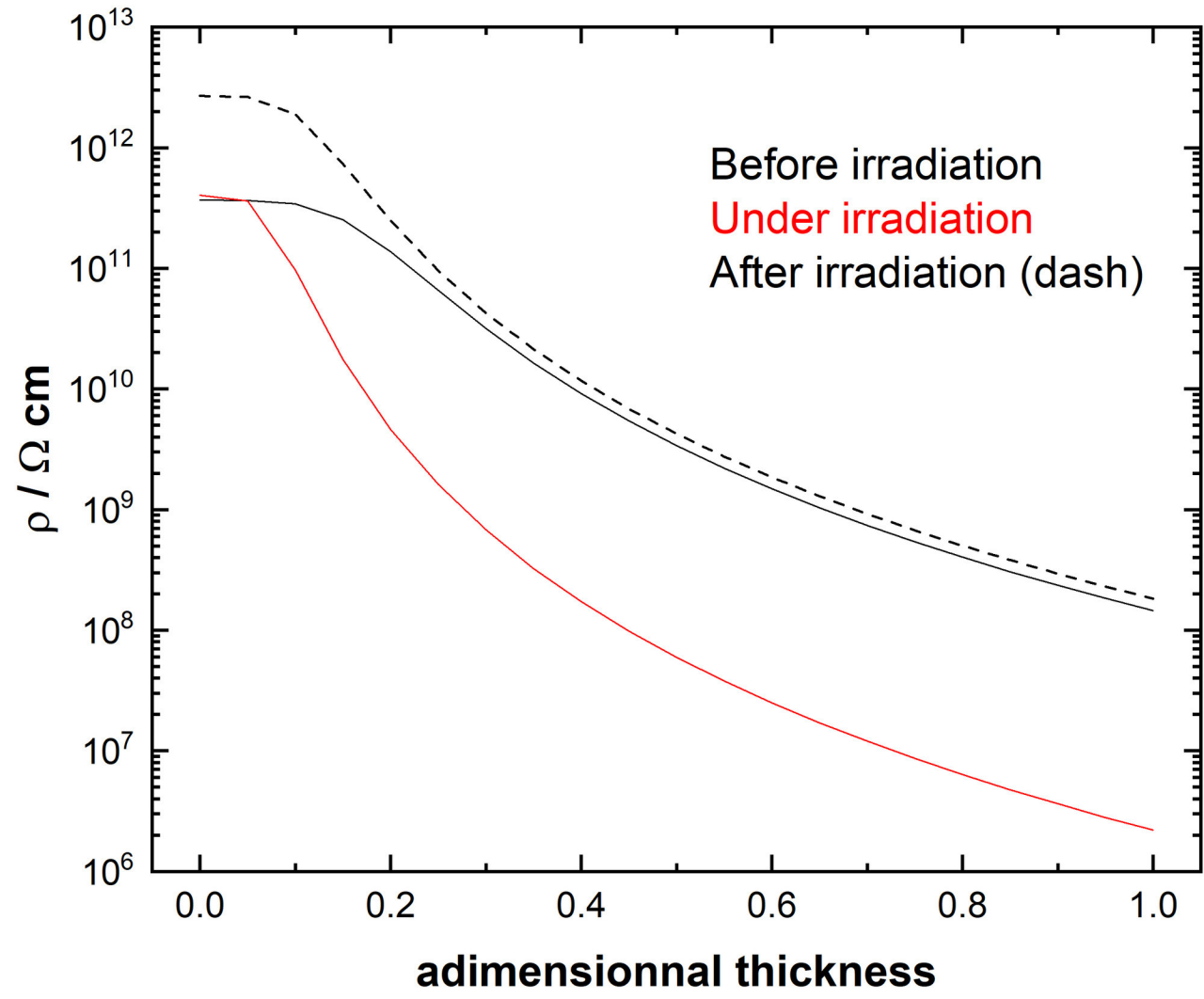
Before irradiation
Under irradiation
After irradiation (dash)
ρ / Ω cm
adimensionnal thickness
10^13
10^12
10^11
10^10
10^9
10^8
10^7
10^6
0.0
0.2
0.4
0.6
0.8
1.0

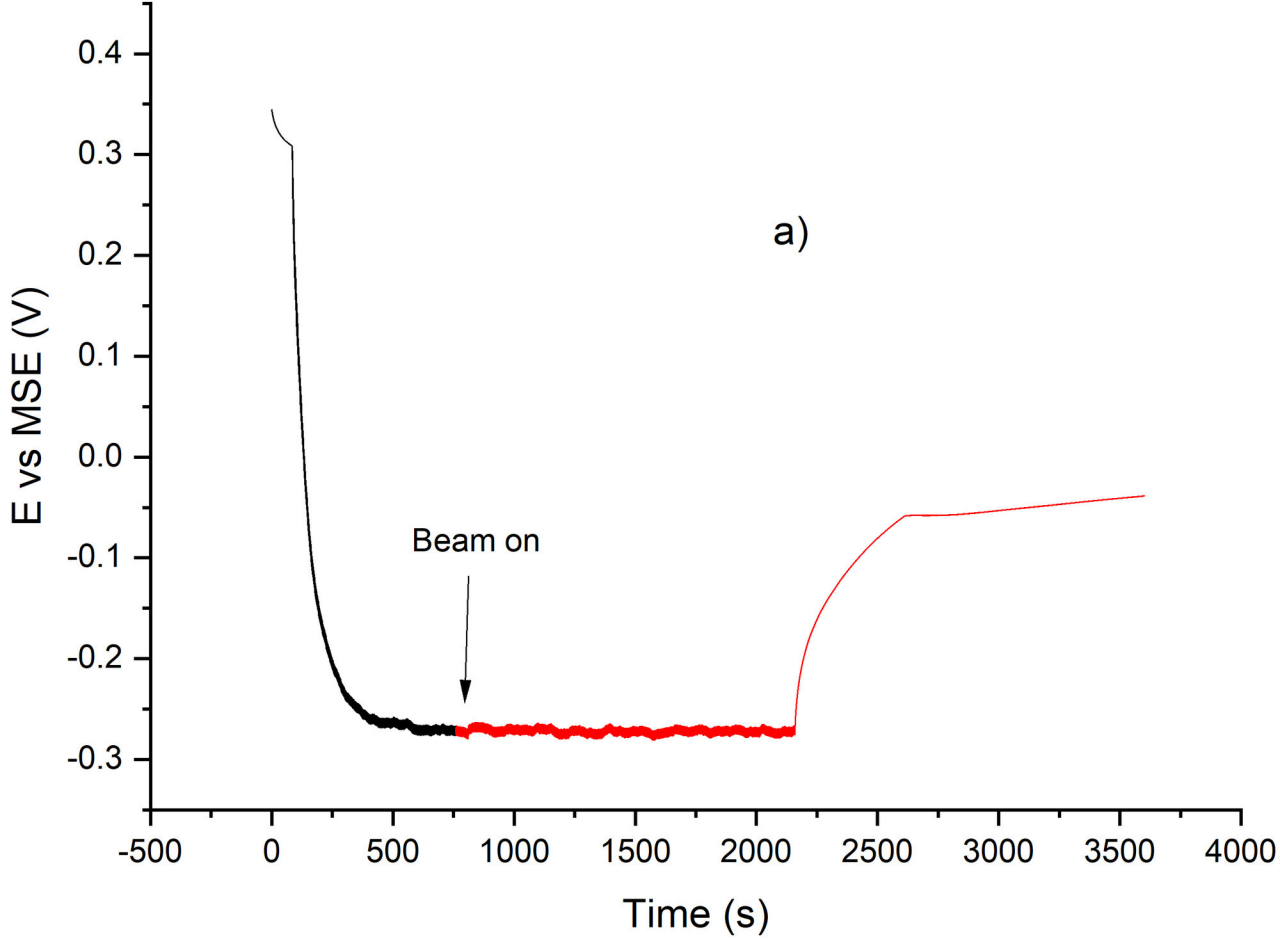
a)
Beam on
E vs MSE (V)
Time (s)
0.4
0.3
0.2
0.1
0.0
-0.1
-0.2
-0.3
-500
0
500
1000
1500
2000
2500
3000
3500
4000

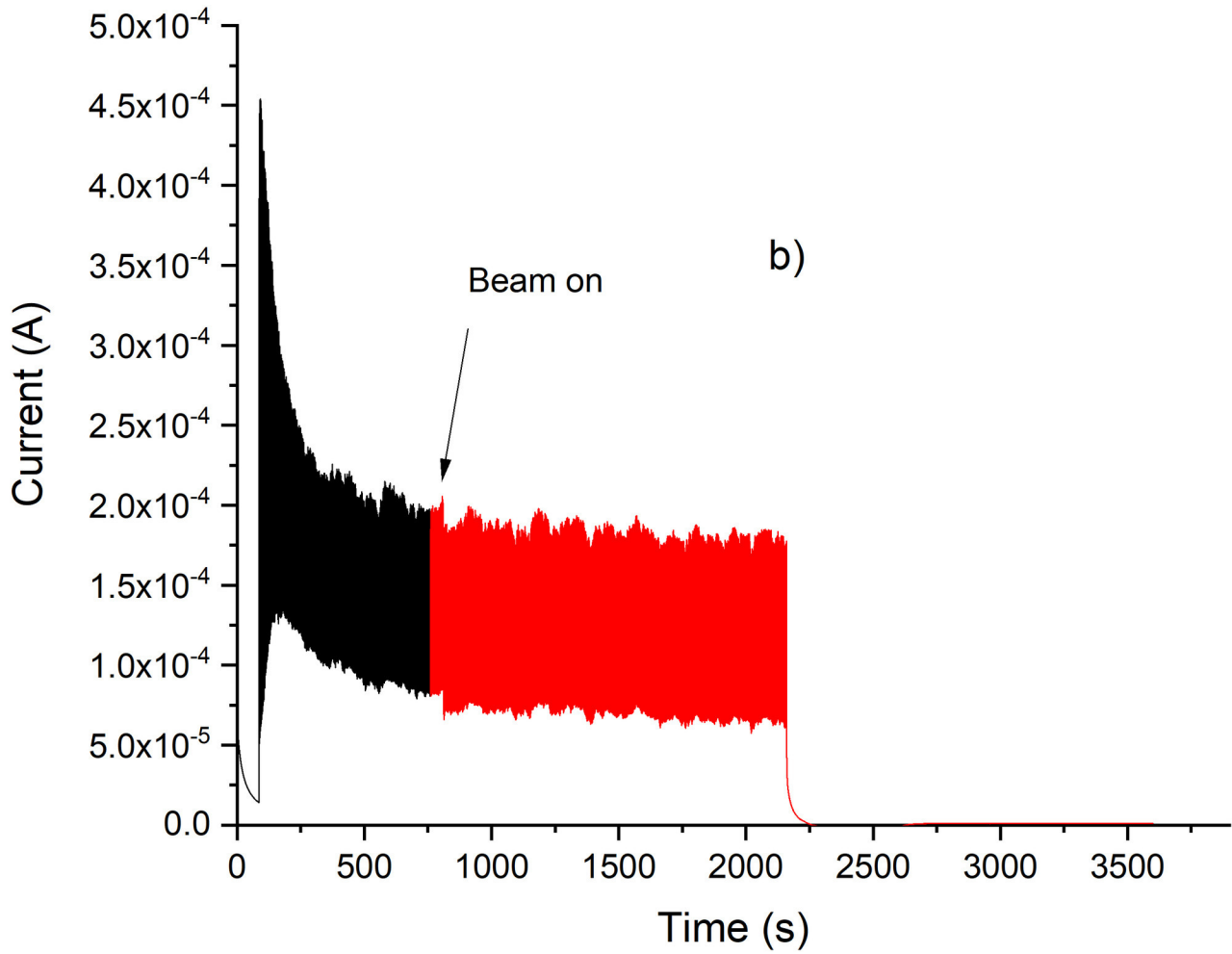
5.0x10-4
4.5x10-4
4.0x10-4
3.5x10-4
3.0x10-4
2.5x10-4
2.0x10-4
1.5x10-4
1.0x10-4
5.0x10-5
0.0
Current (A)
Beam on
b)
0
500
1000
1500
2000
2500
3000
3500
Time (s)

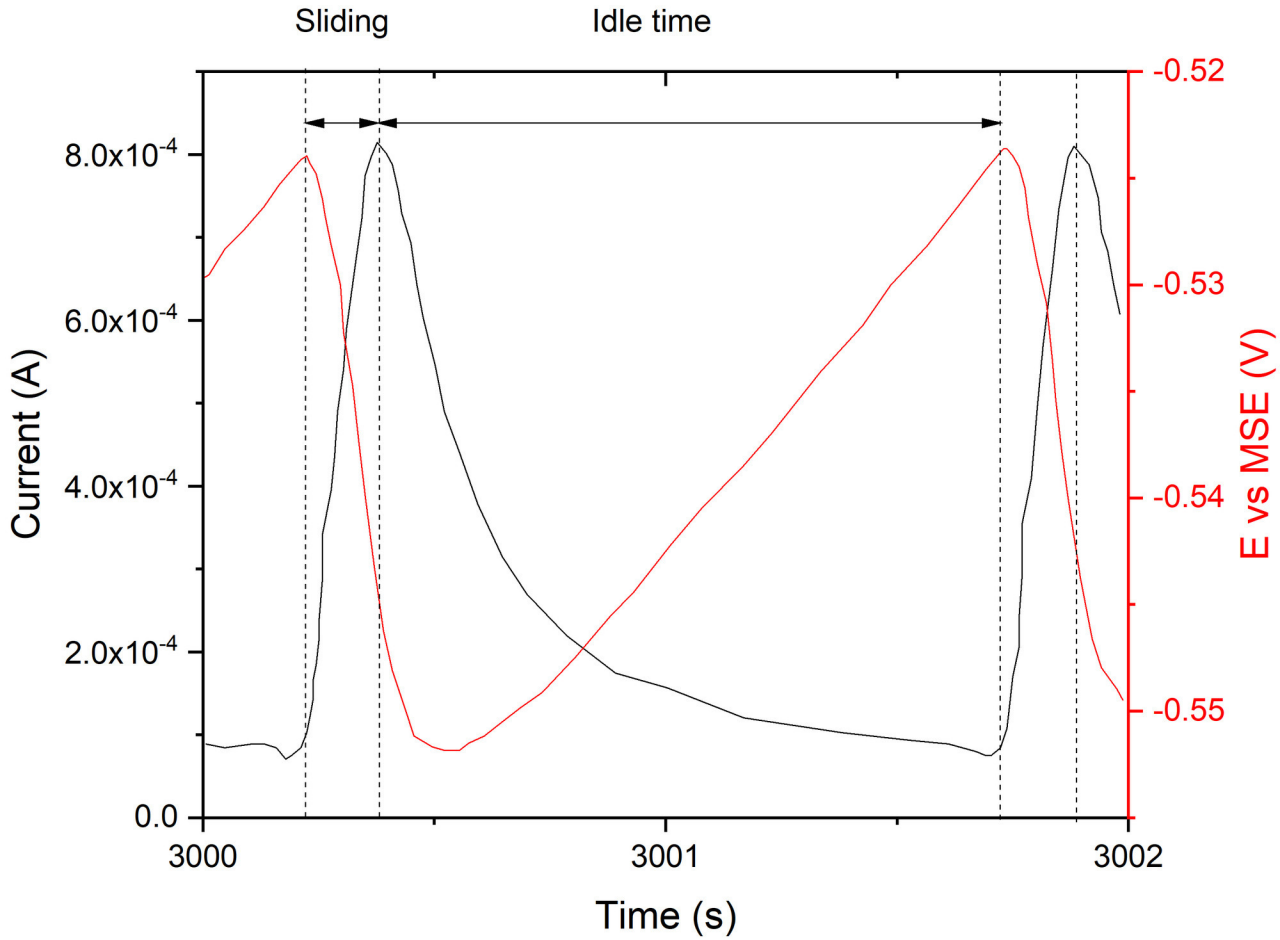
Sliding
Idle time
8.0x10-4
6.0x10-4
4.0x10-4
2.0x10-4
0.0
Current (A)
3000
3001
3002
Time (s)
-0.52
-0.53
-0.54
-0.55
E vs MSE (V)

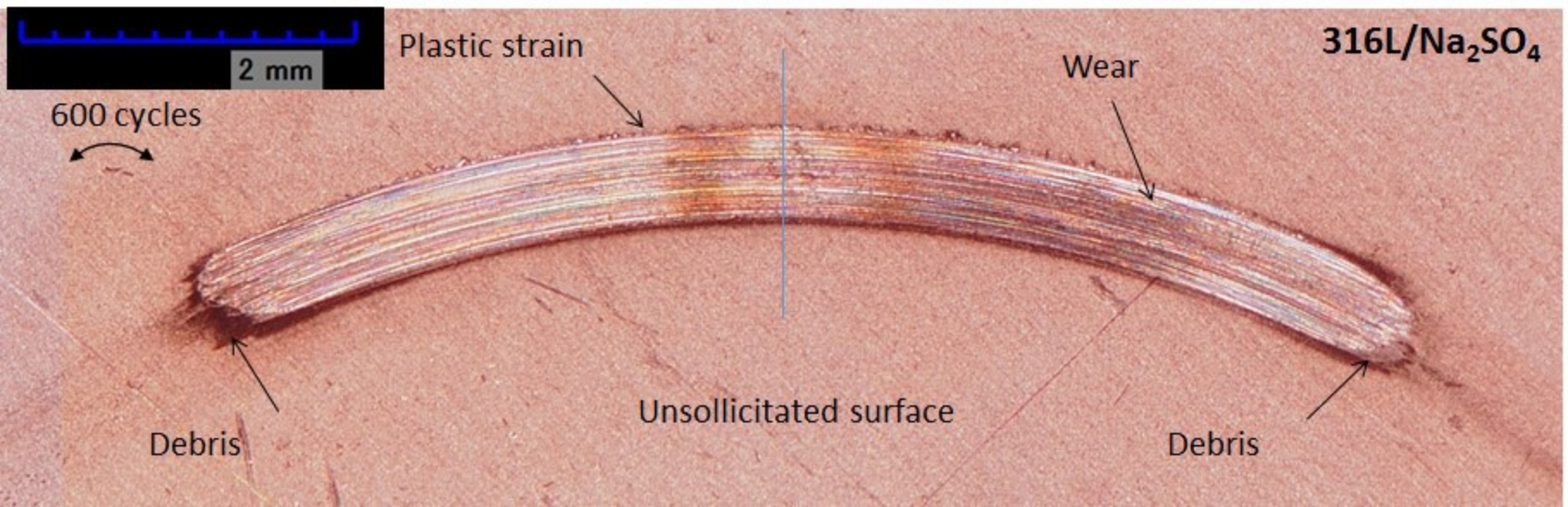
2 mm
Plastic strain
Wear
316L/Na2SO4
600 cycles
Debris
Unsollicitated surface
Debris

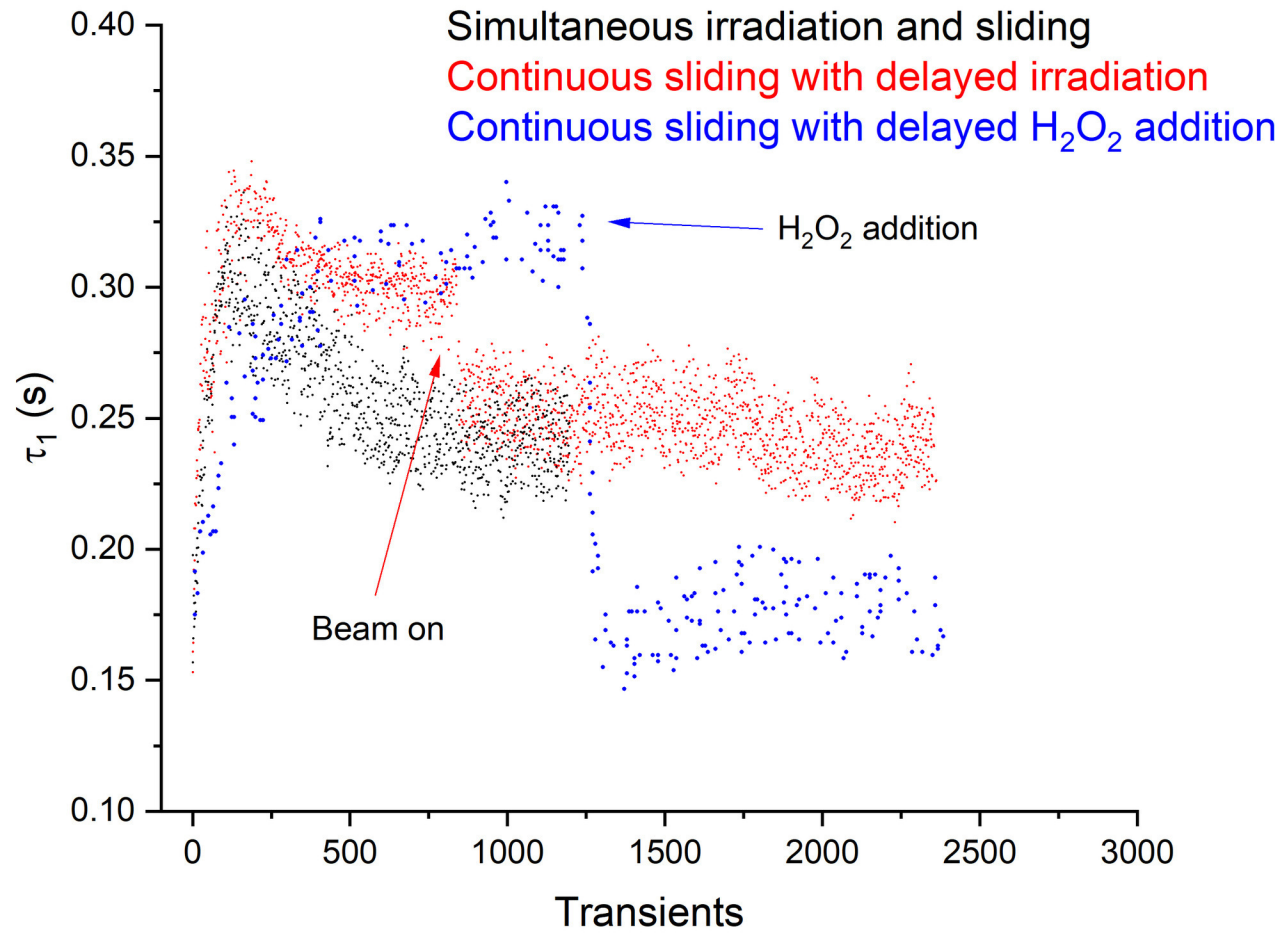
Simultaneous irradiation and sliding
Continuous sliding with delayed irradiation
Continuous sliding with delayed $H_2O_2$ addition
$H_2O_2$ addition
Beam on
$\tau_1$ (s)
0.40
0.35
0.30
0.25
0.20
0.15
0.10
0
500
1000
1500
2000
2500
3000
Transients

**Table 1:** Graphically extracted or fitted parameters obtained from impedance diagrams presented in Figure 11 for the three-irradiation conditions.

| Irradiations conditions | Potential (V vs MSE) | Re ($\Omega.cm^2$) | $\alpha$ | Q ($\Omega^{-1}.cm^2.s^{\alpha}$) | $C_{sc}$ ($F.cm^{-2}$) | $\delta sc$ (nm) | $\rho_0$ ($\Omega.cm$) | $\rho_\delta$ ($\Omega.cm$) |
|---|---|---|---|---|---|---|---|---|
| **Without** | -0.530 | 918 | 0.78 | $1.14\ 10^{-5}$ | $0.8 - 1.8\ 10^{-6}$ | 6-12 | $3.67\ 10^{11}$ | $6 - 140\ 10^{6}$ |
| **During** | -0.315 | 885 | 0.79 | $7.84\ 10^{-6}$ | $3.2 - 8.7\ 10^{-7}$ | 12-33 | $4.04\ 10^{11}$ | $0.1 - 20\ 10^{6}$ |
| **After** | -0.190 | 844 | 0.78 | $1.67\ 10^{-5}$ | $1.1 - 3.6\ 10^{-6}$ | 3-9 | $2.69\ 10^{12}$ | $4 - 577\ 10^{6}$ |